AALTO UNIVERSITY
SCHOOL OF SCIENCE

Koos Zevenhoven

# Solving transient problems in ultra-low-field MRI

Master's thesis submitted in partial fulfillment of the requirements for the degree of Master of Science in Technology in the Degree Program in Engineering Physics and Mathematics.

Helsinki, May 30, 2011

Supervisor:   Professor Risto Ilmoniemi
Instructor:   Professor John Clarke,
              University of California, Berkeley

Magneettikuvausta (MRI) käytetään laajalti kliinisissä sovelluksissa sekä tutkimuksessa. MRI:n valtavirran kehittyessä kohti monen teslan magneettikenttiä on ilmaantunut toinen lähestymistapa, jossa signaali mitataan maan magneettikentän suuruusluokkaa olevassa kentässä ($\sim 100\,\mu\mathrm{T}$). Tällaisen ultramatalan kentän (ULF) MRI:n mahdollistaa erittäin herkkä magneettikenttäanturitekniikka, jonka perustana on suprajohtava kvantti-interferenssilaite (SQUID). Signaalikohinasuhteen (SNR) parantamiseksi näyte esipolarisoidaan korkeammassa kentässä ($\sim 100\,\mathrm{mT}$) ennen jokaista mittaussykliä. ULF-MRI:llä on kiinnostavia ominaisuuksia, kuten ainutlaatuinen kontrasti, turvallisuus, äänetön toiminta, kustannustehokkuus ja yhteensopivuus muun sähkömagneettisesti herkän tekniikan kanssa.

MRI perustuu erilaisiin magneettikenttäpulsseihin ja niiden seurauksena syntyvän ydinmagneettisen resonanssin (NMR) mittaamiseen. Magneettikenttien – erityisesti esipolarisointikentän – pulssitus kuitenkin aiheuttaa useita ongelmia, jotka liittyvät pääosin laitteiston osiin ja niiden ympäristöön kohdistuvaan ei-toivottuun sähkömagneettiseen induktioon. Matalakohinaiseen mittaukseen tarvittavan magneettisuojahuoneen (MSR:n) seiniin indusoituvat pyörrevirrat ovat erityisen vakava ongelma, sillä ne tuottavat magneettikenttätransientin, joka häiritsee mittausta ja vaikuttaa NMR:ään.

Tässä diplomityössä käsittelen pulssien synnyttämien transientti-ilmiöiden aiheuttamia ongelmia sekä niitä yhdistäviä tekijöitä. Sovellan lineaaristen systeemien teoriaa kyseisiin ilmiöihin ja esitän menetelmiä sekä lähestymistapoja niiden lievittämiseksi. Erityisesti johdan transientit ja magneettisen suojauksen selittävän kvantitatiivisen teorian MSR:n seinän pyörrevirroille. Esittämiäni menetelmiä ja lähestymistapoja sovellettiin ULF-MRI-laitteistoon Berkeleyn yliopistossa; laitteistoon tehtiin parannuksia ratkaisuna transienttiongelmiin, jotka estivät uuden kuvanlaatua merkittävästi parantavan kelajärjestelyn käytön. Näiden päivitysten joukossa oli uuden vähäpyörrevirtaisen MSR:n suunnittelu ja rakentaminen. Aikariippuvien pyörrevirtakuvioiden mittaukset käyvät erinomaisesti yksiin esitetyn teorian perusteella laskettujen tulosten kanssa. Lisäksi kuvantamistestien tulokset osoittavat, että tehdyt päivitykset olivat onnistuneita.

Esitän myös transienttienvähennysmenetelmän, jossa ylimääräiset aikariippuvat pulssimuodot kytkeytyvät transientti-ilmiöiden aikakäytökseen. Tämä menetelmä tuo erittäin joustavan tavan kumota samanaikaisesti eri aikaskaaloilla esiintyviä transientteja. Simulaatiotulokset viittaavat siihen, että tällä menetelmällä päästään paljon parempiin tuloksiin kuin millään aikaisemmalla menetelmällä.

| | |
|---|---|
| Author: | Koos Cornelis Jacobus Zevenhoven |
| Degree Program: | Engineering Physics and Mathematics |
| Major subject: | Biomedical Engineering |
| Minor subject: | Physics |

| | |
|---|---|
| Title: | Solving transient problems in ultra-low-field MRI |
| Title in Finnish: | Transienttiongelmien ratkaiseminen ultramatalan kentän MRI:ssä |
| Chair: | Tfy-99 Biomedical Engineering |
| Supervisor: | Professor Risto Ilmoniemi |
| Instructor: | Professor John Clarke, University of California, Berkeley |

Magnetic resonance imaging (MRI) is widely used in clinical applications as well as in research. While the state of the art of MRI has developed towards using multiple-tesla magnetic fields, another approach has emerged, where the signal is measured in a magnetic field on the order of Earth's magnetic field ($\sim 100\,\mu$T). Such ultra-low-field (ULF) MRI is made possible by highly sensitive magnetic-field sensor technology based on superconducting quantum interference devices (SQUIDs). To increase the signal-to-noise ratio (SNR), the sample is prepolarized in a stronger field ($\sim 100\,$mT) before each acquisition cycle. ULF MRI has interesting characteristics including unique contrast, safety, silent operation, and potential in low cost and in compatibility with other electromagnetically sensitive technology.

MRI is based on applying various magnetic field pulses and measuring the resulting nuclear magnetic resonance (NMR) signal. Pulsing magnetic fields, especially the prepolarizing field, however, causes a number of problems, mainly related to unwanted electromagnetic induction to parts of the MRI apparatus and its surroundings. Eddy currents induced in the walls of the magnetically shielded room (MSR), which is required for low-noise measurements, are a particularly serious issue. The eddy currents generate a transient magnetic field, disturbing signal acquisition and affecting the NMR.

In this Thesis, I discuss the problems of pulse-induced transient effects and what they have in common. I adapt theory of linear systems to such effects, and present methods and approaches for suppressing them. In particular, I derive a quantitative theory of eddy currents in the walls of an MSR, explaining transients and shielding. Presented methods and approaches were applied to the ULF-MRI system at University of California, Berkeley; upgrades were made to the system to solve several serious transient issues that prevented using a new coil setup meant to significantly improve the image quality. Among these upgrades, a new MSR with reduced transient eddy currents was designed and constructed. Measurements of the time-dependent eddy-current patterns in the MSR walls show excellent agreement with calculations based on the presented theory. Imaging tests further indicate that the upgrades were successful.

I also present a transient-suppression method, in which additional time-varying pulses are applied in the system to temporally couple to the transient effects. The method provides highly flexible means of simultaneously canceling transients at different time scales. A presented simulation study suggests that this method can yield much better results than any preexisting method.

# Preface

This thesis is based on my visit at University of California, Berkeley in 2010. I experienced some of the greatest times of my life, both scientifically and socially. I had the privilege to work on the pioneering ultra-low-field-MRI system of the Clarke Group, and to implement some of my ideas for solving central issues in the field of research. The research environment, combined with spontaneous after-dinner jam sessions at the International House, and with sunny Sunday afternoons, lying on the grass and playing water games in the pool at Strawberry Canyon, leaves little more to wish for.

The experimental part of this thesis, done in Berkeley, inspired me to develop related theory, which in turn has led to ideas to be implemented in future experiments. I can be nothing but grateful to Professor John Clarke for welcoming me as a visitor in his group, and to Risto Ilmoniemi, our professor at Aalto University, for his part in making this happen.

Much of the experimental part of this work could not have been done without others. I did many measurements together with either Sarah Busch or Fredrik Öisjoen. I'm very grateful for having had Sarah's company and the help of her experience in operating the system and in things such as taming the wild SQUID. I also greatly enjoyed working closely with Fredrik, a visitor from Chalmers, Sweden, during the first few months of my visit. We were indeed called 'Team Scandinavia' by Michael Hatridge, who we were lucky to still have partly working on the MRI project, and of whose previous work the present thesis is, in fact, largely a follow-up. I would further like to thank the undergraduate students Matthew Nichols and Kevin Lee, who were also very helpful as well as enjoyable company.

Additional thanks belong to my Aalto colleagues Jaakko Nieminen, Juhani Dabek, Panu Vesanen and Sarianna Alanko for support and for proofreading my thesis. Finally, I would like to thank my family—and friends, both those I got to know in Berkeley, and those here in Finland.

Helsinki, May 30, 2011

Koos C. J. Zevenhoven

# Contents

# Abbreviations

| | |
|---|---|
| MRI | magnetic resonance imaging |
| NMR | nuclear magnetic resonance |
| ULF | ultra-low-field |
| SQUID | superconducting quantum interference device |
| MEG | magnetoencephalogram |
| SNR | signal-to-noise ratio |
| MSR | magnetically shielded room |
| RF | radio frequency |
| DC | direct current |
| AC | alternating current |
| RFI | radio-frequency interference |
| EMI | electromagnetic interference |
| EMF | electromotive force |
| PVC | polyvinyl chloride |
| Nb | niobium |
| Al | aluminum |
| Ti | titanium |

# Chapter 1

# Introduction

*Magnetic resonance imaging* (MRI) is widely known in clinical use for its contrast between soft tissues and its versatility in both anatomical and functional imaging. It is based on magnetically polarizing the target in an applied magnetic field and measuring the magnetic signal resulting from *nuclear magnetic resonance* (NMR) of magnetized atomic nuclei, typically protons. In proton NMR, the magnetization rotates around the magnetic field $\vec{B}$ at the proton Larmor frequency $f_{\mathrm{L}} = \gamma B$, where $\gamma = \gamma/2\pi = 42.58\,\mathrm{MHz/T}$ is the gyromagnetic ratio of protons [1]. This behavior of the magnetization is often referred to as *precession*, which is due to the direct connection to the quantum mechanical precession of nuclear spin angular momentum.

In virtually all MRI implementations, an applied uniform main magnetic field $\vec{B}_0$ determines the operating frequency. In conventional MRI, $B_0$ is on the order of $1\,\mathrm{T}$, corresponding to the frequency $f_0 = 43\,\mathrm{MHz}$; the radio-frequency NMR signal is measured using induction coils. While the state of the art of clinical MRI has moved towards multiple-tesla scanners, another approach has emerged, where $B_0$ is typically on the order of only $100\,\mu\mathrm{T}$. The interest in such ultra-low-field (ULF) MRI is due to the development of highly sensitive magnetic-field sensors, mainly *superconducting quantum interference devices* (SQUIDs). ULF MRI has advantages, for instance, in its image contrast properties and potential lower cost. It can also be made compatible with *magnetoencephalography* (MEG), *i.e.*, measuring the weak magnetic fields arising from neuronal activity in the brain. [2]

Conventional induction coils detect the rate of change of the magnetic field. Therefore, the signal amplitude is proportional to frequency. A SQUID, however, measures the magnetic field amplitude directly, with no additional dependence on $f$. However, the signal does depend linearly on the field magnitude in which the sample or tissue is magnetized. In regular MRI, that field is $B_0$, but in ULF MRI, this is a clear motivation for using a

technique called *prepolarization*, in which a polarizing field $\vec{B}_\mathrm{p}$ stronger than $\vec{B}_0$ is applied as a pulse before each acquisition step. The magnitude of the precessing nuclear magnetization is then directly proportional to $B_\mathrm{p}$, and so is the *signal-to-noise ratio* (SNR) of the measurement.

As the quality of ULF-MRI images is typically limited by low SNR in the image, one has an incentive to go towards higher polarizing fields. Typical values of $B_\mathrm{p}$ range from tens of millitesla to more than $100\,\mathrm{mT}$. Pulsing a field of such magnitude in a large volume gives rise to a number of problems related to, for instance, the dynamic range of the sensors, or transients caused by coupling of the polarizing pulse to other parts of the system or to the environment.

The highly sensitive measurement requires a *magnetically shielded room* (MSR), which shields the system against external magnetic-field interference. Typically, an MSR is made of aluminum and in many cases additionally $\mu$ metal, which provides shielding at low frequencies down to DC with its high magnetic permeability. However, transient eddy currents induced in the MSR walls by the polarizing pulse can be a major problem for imaging as they cause a magnetic field transient at the sample.

In this thesis, I focus on unwanted transient effects that result from pulsed magnetic fields in ULF-MRI systems. I discuss the theory and practice of tackling these issues by exploiting the underlying physical principles, describe improvements made to the pioneering Clarke-Group ULF-MRI system in Berkeley, and compare them to solutions developed for a hybrid MEG-MRI system at Aalto University.

# Chapter 2

# Ultra-low-field MRI

In this chapter, I introduce concepts related to this work; I discuss principles of prepolarized ULF MRI, SQUIDs, magnetically shielded rooms, and electronics, focusing on the challenges in the field. The basic principles are mostly the same as in conventional MRI, for which an extensive coverage can be found, *e.g.*, in Ref. [1].

Compared to MRI technology currently in use, ULF MRI has a number of potential advantages, including its unique $T_1$ contrast, low cost, safety, silent operation, distortion-free imaging in the presence of metals or tissues of variable susceptibility, and compatibility with other technology such as MEG. These prospects are discussed more comprehensively in the ULF-MRI review by Clarke *et al.* [2].

While the increasing research interest spawns new candidates for ULF-MRI applications, the field still faces major challenges. Many issues arise from the wide range of important magnetic field strengths that span up to 14 orders of magnitude from femtotesla sensor noise levels to polarizing fields around $100\,\mathrm{mT}$. The signal frequency band in the kilohertz range overlaps with the frequency band used in field pulse sequences and waveforms. Consequently, the shielding required for low-noise operation responds significantly also to the applied pulses. It is the same overlapping of bands that also leads to issues related to noise and unwanted transients in ULF-MRI electronics.

## 2.1  Basic principles

In ULF MRI, the measurement field $\vec{B}_0$ and the field $\vec{B}_\mathrm{p}$ that magnetizes the sample are produced by different coils. Typically, the sample is first magnetized by $\vec{B}_\mathrm{p}$ in a direction perpendicular to $\vec{B}_0 = B_0\widehat{e}_z$, for instance, $\vec{B}_\mathrm{p} = B_\mathrm{p}\widehat{e}_x$ ($\widehat{e}_x$, $\widehat{e}_y$, and $\widehat{e}_z$ are unit vectors along $x$, $y$, and $z$ axes). Then, the

proton bulk magnetization $\vec{M}(\vec{r}, t)$, at positions $\vec{r}$ throughout the sample, is brought into precession around $\vec{B}_0$ by one of two methods. In one method [3], $\vec{B}_p$ is switched off non-adiabatically, *i.e.*, so quickly that $\vec{M}$ does not change during the ramp-down, and is left perpendicular to $\vec{B}_0$. In the other method [2], the $\vec{B}_p$ ramp-down is adiabatic, and $\vec{M}$ aligns with $\vec{B}_0$, roughly keeping its magnitude. The magnetization is then flipped by an angle of typically $\pi/2$ by pulsing an excitation field $\vec{B}_1$ tuned to the Larmor frequency $f_0 = \omega_0/2\pi$. The transverse component, *i.e.*, that perpendicular to $\vec{B}_0$ then precesses.

In terms of quantum mechanics, adiabaticity means that, while the proton spin eigenstates change with the changing magnetic field, the individual spin states follow the eigenstates without transitions into other states. Macroscopically, the result is that the magnetization stays aligned with the instantaneous magnetic field. When the direction of the magnetic field $\vec{B}$ turns at an angular rate of $d\theta/dt$, the condition for adiabaticity can be expressed conveniently as

$$\frac{d\theta}{dt} \ll \gamma B \; , \tag{2.1}$$

*i.e.*, the magnetic-field direction changes much slower than the precession angular frequency corresponding to $\vec{B}$.

Non-adiabatic $B_p$ turnoff has the advantage that MRI is possible without a $\vec{B}_1$ coil and excitation pulses. Another feature is that, in the absence of excitation pulses, signal acquisition can be started sooner after polarization. One drawback, however, is that the directional inhomogeneity of $\vec{B}_p$ transfers into the initial phase of the precession, whereas, during adiabatic turnoff, the initial magnetization adopts the homogeneity of $\vec{B}_0$, which can be made much better than that of $\vec{B}_p$. In addition, excitation pulses provide more control over the magnetization than non-adiabatic turnoff.

While precessing, $\vec{M}$ decays to its equilibrium value corresponding to $\vec{B}_0$ according to two relaxation times $T_1$ and $T_2$, which typically range from around $10\,\text{ms}$ up to roughly $1\,\text{s}$ in relevant tissues [1]. The component along $\vec{B}_0$ is governed by the former, and the precessing transverse component $\vec{M}_{xy}$ by the latter time constant. The precessing magnetization gives rise to an oscillating signal that can be measured using a magnetic-field sensor. Because $B_p \gg B_0$, the longitudinal $z$ component is insignificant during the measurement, and $\vec{M}_{xy} \approx \vec{M}$.

The cycle of polarization and measurement of the decaying signal is repeated until enough data have been collected for image reconstruction. The spatial origin of the signal is usually encoded by introducing different magnetic field gradients to the precession field at each cycle. During a gradient pulse, the Larmor frequency depends on $\vec{r}$, which also allows position-

dependent manipulation of the signal phase. A set of three gradient coils is used for producing linear gradients $G_x = \partial B_z / \partial x$, $G_y = \partial B_z / \partial y$, and $G_z = \partial B_z / \partial z$. Also $\vec{B}_1$ pulses together with gradients can be applied for spatial encoding, although slice selection, as often used in conventional MRI, is not as effective in the ULF case. This is because narrow slices require $B_1$ pulses of long durations when the gradient strengths are small. Another reason is that measuring signals from only a selected slice decreases the rate of information acquired. The timings of applied pulses and data acquisition as well as pulse waveforms are determined by the MRI *sequence*, which is set up to acquire the information needed for reconstructing an image of the target.

The magnetization in a differential volume element $dV$ in the target at position $\vec{r}$ contributes to the signal $\psi_{\mathrm{S}}$ seen by a sensor with a sinusoidal component, which can, omitting relaxation for now, be written as

$$d\psi_{\mathrm{S}}(t) = M(\vec{r})|\beta_{\mathrm{S}}(\vec{r})| \cos\left[ \int_{t_0}^{t} \omega(\vec{r}, t')\, dt' + \phi_0(\vec{r}) + \phi_{\mathrm{S}}(\vec{r}) \right] dV \; . \qquad (2.2)$$

Here, $|\beta_{\mathrm{S}}(\vec{r})|$ is the sensitivity of the sensor to a precessing magnetic dipole at $\vec{r}$, $\phi_0(\vec{r})$ is a phase determined by an initial condition at $t = t_0$, and $\phi_{\mathrm{S}}(\vec{r})$ is a phase shift given by the relative positioning of the sensor with respect to $\vec{r}$. The precession angular frequency $\omega(\vec{r}, t) = \omega_0 + \Delta\omega(\vec{r}, t) = \gamma B(\vec{r}, t)$ depends on the applied gradients. The total signal is an integral of $d\psi_{\mathrm{S}}$ over the whole volume of the sample, which can be demodulated with quadrature detection (QD) to obtain a complex-valued signal

$$\psi_{\mathrm{QD}}(t) = \int M(\vec{r})|\beta_{\mathrm{S}}(\vec{r})| \exp\left\{ -i \int_{t_0}^{t} \Delta\omega(\vec{r}, t')\, dt' - i\left[ \phi_0(\vec{r}) + \phi_{\mathrm{S}}(\vec{r}) \right] \right\} dV$$

$$= \int M(\vec{r}) e^{-i\phi_0(\vec{r})} \beta_{\mathrm{S}}(\vec{r}) \exp\left[ -i\vec{r} \cdot \gamma \int_{t_0}^{t} \vec{G}(t')\, dt' \right] dV \; , \qquad (2.3)$$

where $\beta_{\mathrm{S}} = |\beta_{\mathrm{S}}| e^{-i\phi_{\mathrm{S}}}$ is a complex sensitivity factor, and $\vec{G} = G_x \hat{e}_x + G_y \hat{e}_y + G_z \hat{e}_z$ so that the gradient field is given by $(\vec{r} \cdot \vec{G}) \hat{e}_z$.

An interesting property of Eq. (2.3) is revealed by defining a variable $\vec{k}(t) = \gamma \int_{t_0}^{t} \vec{G}(t')\, dt'$. The last expression in the equation is, in fact, the three-dimensional inverse Fourier transform of $M(\vec{r}) e^{-i\phi_0(\vec{r})} \beta_{\mathrm{S}}(\vec{r})$. By applying gradient pulses, one can select points to acquire in the image Fourier space, which is generally referred to as the $k$ space. In a simple sequence, one line of $k$ space is scanned in each acquisition step. This is achieved by applying a so-called frequency-encoding gradient during acquisition. The line of $k$ space to be scanned is selected before acquisition by so-called phase-encoding gradients. A working sequence is presented later, in Chapter 5.

When a sufficient amount of $k$-space data has been acquired, an image can be reconstructed by applying a Fourier transform. Further, if $\beta_S$ and $\phi_0$ are known, one can obtain a uniform-sensitivity image, *i.e.*, the magnitude of the precessing magnetization, $\vec{M}(\vec{r})$. The magnetization is a useful quantity to measure, since it reflects the local properties of the imaging target. Relaxation times $T_1$ and $T_2$ vary between tissue types, and therefore, the magnetizations in different tissues have relaxed to different amplitudes before acquisition. By changing the pulse sequence or its parameters such as waiting times, one can adjust the type of contrast in the image. It has been demonstrated that, at least for some samples, $T_1$ contrast is much better in ULF than in higher fields [2]. Naturally, the magnetization is proportional to the proton density in the target, which also changes from tissue to tissue.

The relaxation of $\vec{M}(\vec{r},t)$ during acquisition leads to broadening of the spectral NMR peak to a line width of $1/\pi T_2$. This effect is called homogeneous broadening and sets a limit to the spatial resolution at least in the frequency-encoding direction. Inhomogeneity in the precession field further causes spins to dephase and increasingly cancel each other over time. As a result, the transverse relaxation time effectively decreases to $T_2^* < T_2$. The corresponding line width increases accordingly. Broadening of the spectral NMR peak due to, for instance, unwanted transient fields or magnetized parts in the system can further limit the available spatial resolution. Therefore, as a rule of thumb, these effects should preferably be kept well below the homogeneous broadening corresponding to relevant tissues.

In practice, the image is obtained in a discretized form consisting of small volume elements, voxels. Consider a voxel of volume $V$ centered at $\vec{r}$. From Eq. (2.3) one can see that the the signal from a voxel is proportional to the voxel volume $V$. Due to noise in the measured signal, the voxel intensity becomes $V\beta_S(\vec{r})M(\vec{r})$ plus a random complex noise term $\xi$ with zero expectation. The sensitivity-corrected voxel intensity is of the form

$$\text{Re}\left( M(\vec{r}) + \frac{\xi}{V\beta_S(\vec{r})} \right) = M(\vec{r}) + \frac{\text{Re}(\xi e^{i\phi_S})}{|V\beta_S(\vec{r})|} \ . \tag{2.4}$$

Assuming that the distribution of $\xi = |\xi|e^{i\phi_\xi}$ does not depend on the phase $\phi_\xi$, the standard deviation $\sigma_\xi$ of $\text{Re}(\xi e^{i\phi_S})$ is independent of $\phi_S$ and proportional to $\sigma_S$, the standard deviation of the noise in the relevant frequency band of the original sensor signal.

The intensity resolution of a voxel is determined by the (amplitude) SNR of the voxel value. The voxel SNR is defined as the correct voxel value $M(\vec{r})$ divided by the standard deviation $\sigma_\xi$ of the random error in the voxel and

can be written as

$$\text{SNR} = \frac{M(\vec{r})V|\beta_{\text{S}}(\vec{r})|}{\sigma_\xi} \propto \frac{B_{\text{p}}V|\beta_{\text{S}}(\vec{r})|\sqrt{T_{\text{tot}}}}{\sigma_{\text{S}}} \ , \tag{2.5}$$

where the last expression incorporates that $M \propto B_{\text{p}}$ and that $\sigma_\xi$ is inversely proportional to the square root of the total MRI scanning time $T_{\text{tot}}$ [1]. It should be recognized, however, that $\sigma_\xi$ also depends on factors not visible in Eq. (2.5), most notably, the imaging sequence, but in general also on $\vec{r}$.

Ultimately, the ability to distinguish between different types of tissue depends on the *contrast-to-noise ratio* (CNR), which can be defined as the SNR of the difference between image values corresponding to two tissues. A better CNR can be achieved by improving either the SNR or the contrast, which strongly depends on the imaging sequence [1].

The only factors in Eq. (2.5) that can be affected by improving the apparatus are $B_{\text{p}}$, $\beta_{\text{S}}(\vec{r})$, and $\sigma_{\text{S}}$. The latter two and the use of arrays of sensors were considered in Ref. [4], whereas the central concept in this thesis is increasing $B_{\text{p}}$ and solving the related problems.

## 2.2 SQUID sensors

SQUIDs are based on *superconductivity*, the phenomenon where the electrical resistivity of a material completely vanishes below a critical temperature $T_{\text{c}}$. A commonly used material that exhibits such behavior is niobium (Nb) which has $T_{\text{c}} = 9.2\,\text{K}$. Superconductor devices are usually cooled by immersing them in liquid helium which boils at $4.2\,\text{K}$. [5]

SQUIDs can be divided into two categories, RF and DC SQUIDs, of which the DC version is typically used in measuring biomagnetic signals [6] as well as ULF MRI [2]. The DC SQUID is a superconducting loop interrupted by two weak links, or Josephson junctions (see Fig. 2.1a). When the SQUID is biased with a suitable current $I_{\text{b}}$, the voltage across the SQUID exhibits a sinusoidal dependence on the magnetic flux going through the loop, which is analogous to the well known double slit interference of waves [5]. The response to magnetic flux is linearized by operating the SQUID in a flux-locked loop [5], where an electronic circuit aims to keep the flux constant by applying negative feedback to the SQUID loop. This is achieved by driving a current to an additional feedback coil $L_{\text{f}}$ that has a mutual inductance $M_{\text{fS}}$ with the SQUID. The signal, which is proportional to the magnetic flux through the SQUID loop, can then be read from the voltage across the series resistor $R_{\text{f}}$.
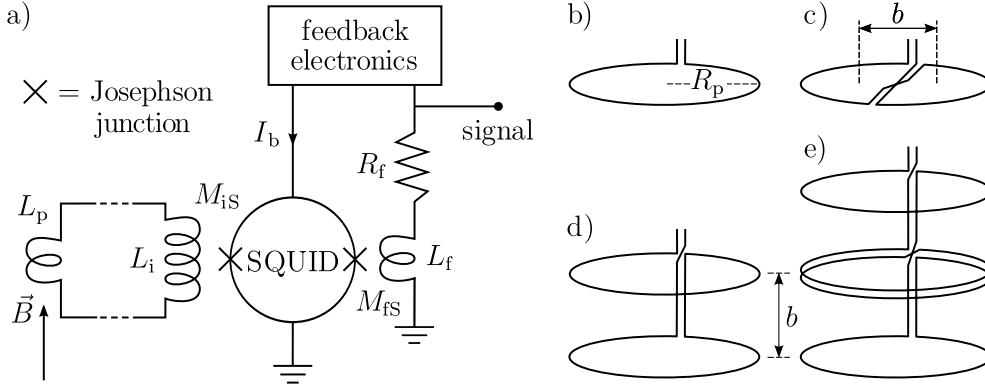
**Figure 2.1:** A schematic illustration of (a) a SQUID sensor and (b–e) pickup coil types, namely (b) magnetometer, (c) planar first-order gradiometer, (d) axial first-order gradiometer, and (e) axial second-order gradiometer.

It is usually advantageous to make the SQUID loop itself small, and couple it to a superconducting *flux transformer* to achieve high sensitivity [5]. The flux transformer, or input circuit, consists of a *pickup coil* $L_p$ connected to an *input coil* $L_i$ (Fig. 2.1) which feeds the SQUID according to the signal received by the pickup coil. The flux transformer forms a continuous superconducting path, which, by nature, conserves the flux through itself.

Different types of responses to magnetic fields can be achieved by varying the pickup-coil geometry. Figure 2.1b–e schematically describes some of the most popular types. The simplest case is just a single loop, a *magnetometer*, which in a homogeneous field responds linearly to the field component perpendicular to the plane of the loop (b). Two parallel loops wound in opposite directions and connected in series can be used to form a *gradiometer*. The resulting signal is that of one loop subtracted from the other. It can be used to approximate a derivative of the field component with respect to the direction in which the loops are displaced (by distance $b$, called the baseline). Typical examples are the planar gradiometer (c) and the axial gradiometer (d). By using more loops, one can measure higher-order derivatives. Well-known ULF-MRI implementations [2, 7] currently use second-order axial gradiometers (e) because of their ability to suppress noise or interference originating from distant sources.

Consider a pickup coil with inductance $L_p$ connected to an input coil with inductance $L_i$. The two together form an untuned input circuit whose inductance is $L_i + L_p$, if one neglects the parasitic inductance of the leads connecting the pickup and input coils. When the magnetic flux through the pickup loop due to the signal source changes by $\delta\Phi_p$, there is a corresponding change $\delta J_i$ in the supercurrent flowing in the input circuit. The magnitude

and direction of $\delta J_i$ are such that the flux through the superconducting input circuit remains constant, *i.e.*, $\delta\Phi_p - \delta J_i(L_p + L_i) = 0$. One thus obtains $\delta J_i = \delta\Phi_p/(L_p + L_i)$. The change in the flux through the coupled DC SQUID loop is then given by

$$\delta\Phi_S = M_{iS}\delta J_i = \frac{M_{iS}}{L_p + L_i}\delta\Phi_p \;, \tag{2.6}$$

where $M_{iS}$ denotes the mutual inductance of the input coil and the SQUID. Further, $M_{iS}$ can be expressed in terms of $L_i$ and the inductance $L_S$ of the SQUID loop as [5]

$$M_{iS} = k\sqrt{L_S L_i} \;. \tag{2.7}$$

The coupling coefficient $k$ has a value between $-1$ and $1$, that depends on the geometry.

SQUID sensors are most typically configured for low noise. For a given pickup coil and SQUID, the number of turns in the input coil can be designed to provide optimal coupling of the desired signal to the SQUID. By making the simplifying assumption that $k$ and $L_S$ are independent of the number of input-coil turns, the best coupling is obtained when $L_i = L_p$ [8]. If the noise of the SQUID or its electronics is dominant and likewise independent of the input coil, this selection gives the best magnetic-flux resolution, which is proportional to $\sqrt{L_p}$. Since $L_p$ is roughly proportional to the pickup-coil size $R_p$, the flux resolution scales as $\sqrt{R_p}$, and the field resolution as $R_p^{-3/2}$. For low-noise magnetic-field measurements, the pickup coil should thus be made large. Even with a fixed input coil, the sensitivity increases with pickup-coil size, since $\delta\Phi_p \propto R_p^2$ for a single loop.

The noise properties of the DC SQUID are also affected by radio-frequency interference (RFI) [9]. Exposure of the SQUID to RFI effectively decreases the amplitude of the flux-to-voltage curve at low frequencies, which, if the voltage noise is constant, leads to corresponding decrease in the field resolution of the sensor. While there are approaches to increasing the RFI-tolerance of the setup [10], shielding is required. The authors of Ref. [9] report that an attenuation of 60 dB was required for their setup and environment in Tokyo. Attention must be paid to RFI in designing ULF-MRI systems—especially because the coils require high-current and high-voltage lines, which can be difficult to filter.

ULF MRI is a challenging setting for SQUID sensors. Although the SQUID itself can be enclosed in a superconducting shield, the pickup coil is always exposed to the pulsed magnetic fields required for MRI. Especially the strong polarizing field can cause magnetic flux to be trapped in superconducting parts, hampering subsequent measurements. An elegant solution

is to add a flux dam, that is, an array of Josephson junctions, in series with the input circuit. Below the critical current of the junctions, the circuit is superconducting. If, as a result of a pulsed magnetic field, the critical current is exceeded, the junctions switch to the normal state, limiting the buildup of current [2]. When the magnetic field has returned to within the dynamic range of the sensor, the Josephson junctions are again superconducting, and the sensor is again functional.

## 2.3   Magnetically shielded rooms

To make use of the high sensitivity of the sensors, environmental magnetic noise must be eliminated. While gradiometric pickup coils can be used for canceling out external noise, additional shielding is often required, not only in the measurement band, but also against RFI, as discussed above. Noise at any frequency should also not exceed the dynamic range of the sensor and its electronics. For ULF MRI, an additional requirement is that external magnetic-field noise does not change the precession field and thereby affect the spin dynamics of the sample. Different approaches can be used in magnetically shielded rooms to meet these requirements.

Materials with high electrical conductivity $\sigma$ or those with high magnetic permeability $\mu$ are effective as passive shielding against electromagnetic interference (EMI). The former act through currents induced in them by an external time-varying interference field; the currents give rise to a field which cancels the interference to some accuracy. This effect is zero for static magnetic fields, but increases with frequency. Highly permeable ferromagnetic materials, on the other hand, offer a low-reluctance path for the magnetic flux, guiding the flux lines around the target volume within the MSR walls. Even DC fields such as Earth's magnetic field are suppressed. However, at high frequencies ($> 10\,\mathrm{kHz}$), conductivity-based shielding can be more effective.

These differences make the choice of materials and design for an MSR strongly dependent on the specific application. A copper or aluminum shield with a thickness of several millimeters can be more than sufficient for a high-frequency application. Low-frequency measurements such as MEG ($<$ $1\,\mathrm{kHz}$), on the other hand, could be conducted in an otherwise similar shield but made of $\mu$ metal, which is a high-permeability alloy containing mainly nickel and iron, with $\mu$ on the order of $10^4\mu_0$ [11]. Still, $\mu$-metal rooms typically contain layers of aluminum as well, not only because of added AC shielding, but also because of better mechanical properties of aluminum [12].

In order to reach large shielding factors, most MSRs are designed to fully

enclose the target volume. This is particularly true for conductivity-based shielding, where imperfections in joining the sheet metal can add significant resistance in current paths. In high-performance MSRs, the seams between individual wall plates are therefore welded together carefully [13]. It is often stated in literature that spherical shields are more effective than rectangular ones [5, 12]. Still, the former type is usually impractical—not least because of the large number of seams resulting from approximating a sphere by a polyhedron. It is also common to use multiple combined aluminum–$\mu$-metal layers with some spacing in between, which increases the shielding factor more than doubling the layer thickness [14].

For biomagnetic measurements and ULF MRI, typical shielded rooms measure several meters in each direction and can be walked into. The weakest spot is usually the entrance; openable connections between plates are likely to have a much higher resistance than fixed seams. There is a multitude of commercial EMI gaskets designed for sealing up openable seams. Such gaskets are conducting flexible strips that ensure that there is electrical contact throughout the length of the seams, while requiring a relatively low applied pressure. In terms of shielding, such contacts are effective mostly for high frequencies, providing at least the RF shielding required for SQUID operation. At low frequencies, however, the door impairs the conductivity-based shielding, and introduces asymmetry in the room and its response.

Although the purpose of a shielded room is to respond to external sources and to cancel their field inside the shielded volume, there is no real distinction between internal and external sources. Hence, the magnetic fields due to internal sources are distorted in time and space compared to those in infinitely extending free space with $\mu = \mu_0$ and $\sigma = 0$. When working in a small volume close to the center of the room, the effect of the room is orders of magnitude smaller than the direct field from the source. For instance, neural currents in MEG produce such weak fields that the resulting 'MSR effect' is likely to be drowned in noise. Moreover, there are other uncertainties that make such small deviations insignificant. In prepolarized ULF MRI, however, the pulsed fields differ from the precession field by a factor typically around $10^3$, and from the measurement noise levels by a factor as high as $10^{14}$. As a result, the MSR affects not only the measurement but also the spin dynamics in the sample. This has proven to be a common issue impeding the development of ULF-MRI and combined MEG and MRI [15, 16].

Most problematic is the conductive shielding. Eddy currents induced in the shield hold inductive energy, which is mostly dissipated in the shield by the ohmic nature of the currents. As a highly simplified model, the eddy currents can be considered an electrical circuit with resistance $R$ and inductance $L$. If a current $I$ in the polarizing coil, having a mutual inductance

$M$ with the shield, is ramped down to zero, the resulting electromotive force (EMF) in the shield is $MdI/dt$. At the end of the ramp-down, the EMF has built up a current in the shield, which subsequently decays exponentially with the time constant of the circuit, $L/R$, as does the resulting magnetic field. In this view, it is clear that using a thick conductive shield with high-quality weldings leads to a small $R$ and long transients after pulses.

Ideally, permeability-based shielding has no time-dependent behavior, that is, it only affects the spatial profiles of the instantaneous applied field. For ULF MRI, this is an attractive property, since there are no transients after pulses. Additionally, $\mu$ metal as the innermost layer will screen an outer conductive layer from the pulsed fields, reducing the eddy-current transient. In reality, $\mu$ does have a frequency dependence, which implies a corresponding transient behavior. Moreover, $\mu$ metal itself is conductive, although to a much lesser extent than aluminum.

For MEG, shielding at frequencies down to nearly DC is vital. Therefore, it is natural for a hybrid MEG-MRI system to have $\mu$-metal layers in its MSR, although there are several drawbacks. Being exposed to relatively strong applied magnetic fields can lead to persistent magnetization of the $\mu$ metal, which degrades its performance and causes residual DC fields in the room. This may introduce the need for an easily accessible degaussing procedure. Added to that, the price of $\mu$ metal is high and it adds to the weight and complexity of the system.

When not using $\mu$ metal, Earth's field needs to be taken care of. One way is to orient $\vec{B}_0$ and the whole system along Earth's field. A more flexible way is to cancel the field using additional coils. Another possible issue can be external low-frequency magnetic fields that affect the NMR. In principle, the problem can be solved by active shielding [17], that is, by feeding appropriate time-varying currents in a number of coils such that the external field is canceled to a sufficient accuracy in the imaging volume. However, the implementation of such feedback can be difficult for reasons that include noise and phase-shift issues as well as problems related to mutual inductances between coils, which will be discussed in later sections.

## 2.4   Electronics for driving coil currents

The issues of noise and unwanted transients also affect the electronics that pulse and regulate currents in coils.

Even without these issues, the coil inductances make pulsing the coils somewhat challenging. The voltage over a coil of resistance $R$ and inductance $L$ when it is fed with a current $I(t)$ is $U = RI + LdI/dt$, where the second

term is the self-induced EMF. Especially with pulsed polarizing coils, the peak value of the second term can be very high compared to the first term. For instance, a coil with $L = 100\,\text{mH}$ and $R = 1\,\Omega$ ramped up to $I = 100\,\text{A}$ in $10\,\text{ms}$ yields $RI = 100\,\text{V}$ during the on-state and $LdI/dt = \pm 1000\,\text{V}$ during ramps. The peak power output from the current source producing the pulse would be as high as $100\,\text{kW}$. A power supply with such high power output, however, would be expensive and overkill, since during the on-state at $100\,\text{A}$, the required power is an order of magnitude lower.

One solution to this problem is described in Ref. [18]; the inductive energy $LI^2/2$ in the polarizing field during the pulse is stored into a capacitor bank $C$ during ramp-down and fed back into the coil during the next ramp-up. This is achieved by switching the coil in series with $C$ to form an oscillating $LC$ circuit for a quarter cycle during each ramp. The result is a ramp-up shaped approximately as the function $\sin(x)$ with $x \in [0, \pi/2]$ and a ramp-down of the same shape but reversed in time. The additional voltages for ramps are thus fully provided and withstood by the capacitor bank and coil, which reduces the power requirement to $10\,\text{kW}$ in the above example.

The same problem applies to pulsed gradients as well, but here, as simple a solution cannot be used because of the need of arbitrary waveforms, or at least of programmable amplitudes. Fortunately, if long ramp times of several milliseconds are tolerated, the issue is minor.

Another issue is magnetic-field noise coming from noise in coil currents. The coils in which no current flows during signal acquisition can be temporarily disconnected using relays, which eliminates the noise issue. However, coils such as those for $B_0$, frequency-encoding, or Earth's-field cancellation will be on while signals are recorded, and low-noise current sources are needed. For instance, a coil that produces $10\,\text{µT/A}$ should have a white-noise level as low as $100\,\text{pA}/\sqrt{\text{Hz}}$ to not exceed the sensor noise. Harmonics of $50/60\,\text{Hz}$ can be an even larger problem.

The use of gradiometers greatly alleviates these issues. Still, for low-noise current sources, one typically uses regulated DC supplies, which sets restrictions to sequence design, and can lead to image artefacts. Such supplies typically also have long transient-recovery times, since low noise and active current sourcing are difficult to achieve in the same frequency band. Long transient-recovery times can be very harmful, since EMFs induced in the coil by other pulsed coils leave long current sweeps in the DC supplies. At Aalto University, we have been working on solving these issues by electronics, which will be the topic of Sarianna Alanko's upcoming Master's thesis. In later chapters of the present thesis, I also discuss solving these issues with existing current sources.

## 2.5   Berkeley system

Although SQUID-detected NMR [19] and prepolarized MRI [20] had been studied earlier, it was not until the concept of prepolarized SQUID MRI, established at University of California, Berkeley [21], that ULF MRI became an increasingly popular research field. Many of the advantages mentioned in the beginning of this chapter were originally demonstrated with the Clarke-Group system in Berkeley. In this section, I will describe the system, leaving upgrades made during this thesis work for the discussion starting in Chapter 4.

The Berkeley ULF-MRI system (Fig. 2.2) is based around a single DC SQUID coupled to a wire-wound second-order axial gradiometer pickup coil such as in Fig. 2.1e. The gradiometer has a baseline of 75 mm and a loop diameter of 63 mm. The SQUID chip itself is on a small circuit board inside a superconducting niobium can, which is at a distance above the gradiometer so that it does not significantly distort the flux seen by the pickup coil. In series with the input circuit, there is, as explained in Section 2.2, an array of Josephson tunnel junctions to limit the current and thereby the flux coupled to the SQUID inside the Nb container.

The estimated balance of the present gradiometer is over 1000, *i.e.*, the response of a perfectly uniform field is canceled to within a part in 1000 by the gradiometric configuration compared to that seen by just a single loop as a magnetometer. This gives a high shielding factor against external noise, since the field from a distant source is nearly uniform.

The described SQUID setup is kept at 4.2 K inside a cylindrical liquid helium cryostat built in the Clarke Group based on the design by Seton et al. [22]. The design provides ultra-low thermal magnetic noise, such that the cryostat noise is not dominating. The full helium volume is about 4 liters, which boils off in roughly 40 hours.

The cryostat and the coils are supported by a wooden structure, as illustrated by Fig. 2.2. The $B_0$ field and encoding gradients are all generated by pairs of planar coils positioned symmetrically around, and parallel to, the $xy$ plane. Each pair is connected in series. The circular coils generate $B_0$ along the $z$ axis, and the outer pair, with currents in opposite directions, is for creating a $\partial B_z/\partial z$ gradient. In between, there are two coils for $\partial B_z/\partial x$ and $\partial B_z/\partial y$. The polarizing coil and the sample, which is on top of the coil, are right under the cryostat close to the lowest loop of the gradiometer. Along the $y$ direction, there is a Helmholtz coil for applying $B_1$ pulses.

In addition to the MRI coils, on the outside of the cubic structure, there are pairs of square shielding coils for canceling Earth's static magnetic field. In the $z$ direction the coils are not needed since the current in the $B_0$ coil

$B_x$, $B_y$ cancellation coils

low-noise cryostat

gradiometer (and SQUID)

$dB_z/dz$ gradient coil

$dB_z/dx$ gradient coil

$\vec{B}_0$ coil (measurement field)

polarizing coil and sample

$\vec{B}_1$ coil (excitation field)

$dB_z/dy$ coil omitted for clarity
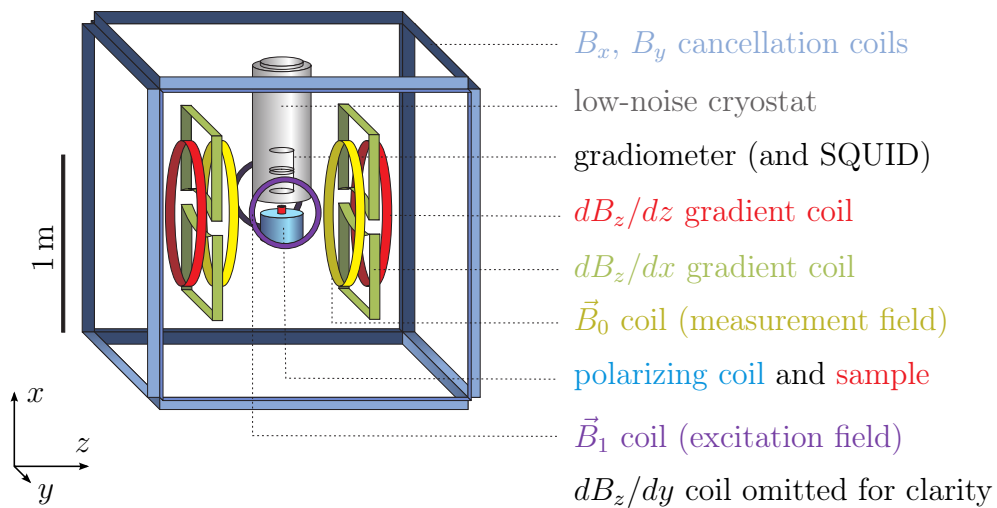
1 m

$x$

$z$

$y$



**Figure 2.2:** The part of the Berkeley setup that is inside room illustrated schematically and as a photograph. [23]

can be adjusted accordingly.

Screening the AC fields is achieved by a cubic aluminum shielded room that surrounds the wooden structure. The previous-generation room had dimensions $2.44 \times 2.44 \times 2.44\,\mathrm{m}^3$ ($8^3\,\mathrm{ft}^3$), and was made of 6.4-mm-thick (1/4") aluminum plates. The plates were bolted tightly to a frame made of hollow aluminum bars, using a large number of brass bolts. Even without welded seams, some shielding was achieved at fairly low frequencies such as $60\,\mathrm{Hz}$. Consistently, the shielding in the measurement band, around $5.6\,\mathrm{kHz}$, easily exceeded the requirements of the measurement. [24]

As mentioned in Section 2.3, effective conductive shielding does have its downside—transients. The polarization coil that had been used in this shielded room, however, had quite small an effective area, leading to a small magnetic dipole moment per unit $B_\mathrm{p}$. Although the polarizing fields were up to over $100\,\mathrm{mT}$ in a small volume, the eddy currents resulting from the ramp-down were not strong enough to impair most MRI sequences used.

The replacement of this coil with a larger one more suitable for larger samples, however, resulted in a severe transient of over $150\,\mu\mathrm{T}$ and a time constant of $50\,\mathrm{ms}$. The transient is stronger than the measurement field itself, making normal ULF-MRI practically impossible. A large part of this thesis is devoted to solving the problems arising from upgrading to higher $B_\mathrm{p}$ and larger polarizing coils.

## 2.6  Aalto system

At Aalto University, we have designed and built an ULF-MRI system as part of an EU-funded project aimed at developing a hybrid MEG-MRI scanner prototype. The system is in many ways similar to that in Berkeley, but has some considerable differences. The setup is currently undergoing major upgrades. In this section, I will briefly describe its state in 2010.

As in the Berkeley system, the main MRI coils are arranged in pairs of vertical planar coils, leaving space in between for the cryostat, polarization and excitation coils, and the sample or subject. The coil structure is depicted by Fig. 2.3 along with a photograph of the system, showing the wooden structure supporting the PVC coil frames. The polarization coil has a structure to minimize its interaction with the shielded room, as will be discussed in some more detail in Section 3.1. The coil currents are controlled by designated electronics, which will be described in other reports.

Making the system suitable for MEG gives rise to at least two additional requirements. The first is that multiple sensor channels are needed for solving the so-called MEG inverse problem. In fact, the use of multiple channels can
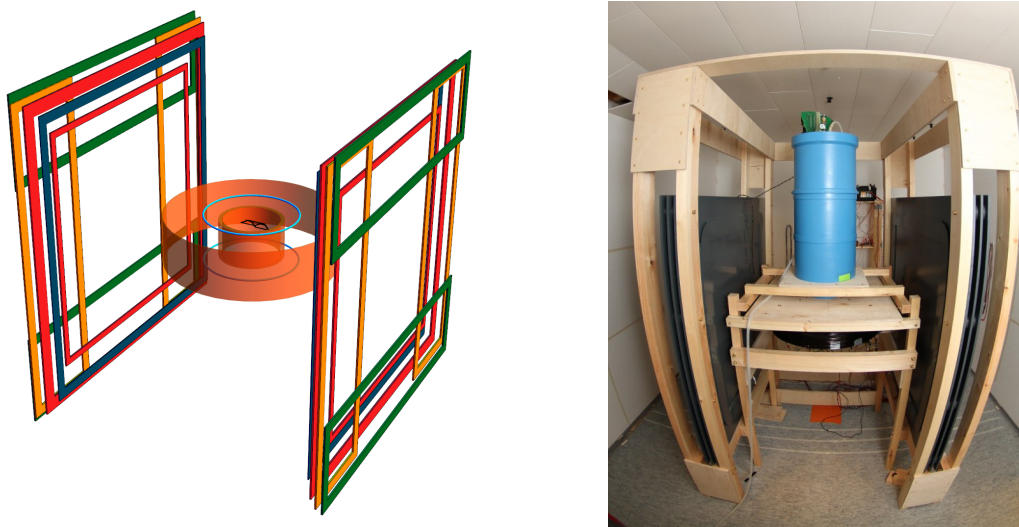
**Figure 2.3:** Schematic illustration of the coil structure in the Aalto 2010 test system and a photograph of the system. The image deformation is due to using a fisheye lens to obtain a wide enough field of view inside the shielded room. [25]

be advantageous for ULF MRI as well, as is discussed more thoroughly in Ref. [4]. The Aalto system has been used with up to eight channels; the goal is to eventually have a 'whole-head' sensor array for both MEG and ULF MRI. The field-tolerant SQUID sensors have been developed for the project by VTT and Aivon Oy [26]. The pickup coils are planar magnetometers (Fig. 2.1b) and gradiometers (Fig. 2.1c) with rectangular loops produced by niobium thin-film technology on a $28 \times 28 \,\text{mm}^2$ silicon wafer. The SQUID chip itself is attached to the center of the pickup chip.

The second MEG requirement is that the shielded room must provide sufficient shielding even at low frequencies down to DC. For this reason, the system is inside an MEG-optimized MSR with two layers of 1-mm-thick $\mu$ metal and 8-mm-thick aluminum each. Here, the longest time constants are long, on the order of a second, but because the inner part of each layer is $\mu$ metal, the amplitude of the eddy-current transient is suppressed (see Section 2.3). Although the transient problems in the Aalto and Berkeley systems have partly different characteristics, many of the principles in solving the issues can be applied to both types of systems.

# Chapter 3

# Transients and shielding

Electromagnetic induction plays a significant role in most aspects of ULF MRI. While even principles behind NMR and its detection by SQUID sensors fit under a loose definition of electromagnetic induction, more direct examples are the effects of self- and mutual inductances of the various coils in the system. Furthermore, magnetic shielding by conducting materials is based on Faraday's law and induced currents.

As mentioned earlier, Faraday induction has its unfortunate side effects, which include transients that decay at time scales comparable to those in ULF-MRI sequences, or larger. Whether the transients sustain as eddy currents or as a recovery transient of the coil-driving electronics, it is common to observe exponentially decaying magnetic fields. Decaying oscillations are also a temporal profile seen in, for instance, the responses of electronics.

The described responses are typical of linear systems. A differential equation of the form

$$c_1 \frac{d}{dt} x(t) + c_0 x(t) = f(t) \qquad (3.1)$$

is a simple example of such a system. The simplified LR circuit model for a conductive magnetically shielded room, as described in Section 2.3, also takes the form of Eq. (3.1), when $c_1 = L$, $c_0 = R$, and $x(t) = j(t)$ is the current in the circuit. The function $f(t)$ is an externally applied voltage which can be considered the input signal of the system. In the MSR transient example, it is the EMF induced by the current $I_\mathrm{p}$ in the pulsed coil, $f(t) = -M dI_\mathrm{p}/dt$. To the corresponding homogeneous equation, $i.e.$, setting $f(t) = 0$, the solution is $x(t) = x_0 e^{-\frac{t}{\tau}}$, where $\tau = c_1/c_0 = L/R$, and $x_0$ is determined by the initial condition $x(t_0) = x_0$. This is the exponential decay that occurs after energy has been brought into the system by $f(t)$.

An LR circuit can also be used as a filter. In this case, $f(t) = u_\mathrm{in}(t)$ is the input voltage to be filtered. The response of an LR low-pass filter is given as

a function of the angular frequency $\omega$ by

$$\hat{u}_{\text{out}}(\omega) = R\hat{j}(\omega) = \frac{1}{1 + i\tau\omega}\hat{u}_{\text{in}}(\omega) \ , \tag{3.2}$$

where the hat denotes the temporal Fourier transform. At low frequencies, $\tau\omega \ll 1$, the output is equal to the input, $\hat{u}_{\text{out}} = \hat{u}_{\text{in}}$. However, at high frequencies, $\tau\omega \gg 1$, the response is $\hat{u}_{\text{out}} = -\frac{i}{\tau\omega}\hat{u}_{\text{in}}$. The output is thus inversely proportional to the frequency, and the phase is delayed by $\pi/2$. In between is the $-3$-dB point given by $\tau\omega \approx 1$.

The simple differential equation discussed above is of great relevance to this work, although more complex models are in order. In this chapter, I will describe such models and their applications in solving transient problems in ULF MRI. While this theory can explain transients in eddy currents and in current-source electronics, it is also shown how the LR filter example is in fact a simplified analogy of the magnetic screening provided by a conductive shield. The considerations of this chapter can be used as a basis for understanding the upgrades to the Berkeley ULF-MRI system (Chapter 4) and for solving future transient problems.

## 3.1 Reducing the cause of transients

At first, I will discuss a direct approach to eliminating transients, for which the above first-order model is sufficient, although the system can be much more complex, even nonlinear. The external driving term, $f(t)$, is what excites the system, and afterwards, when $f(t) = 0$, leaves it in an exponentially decaying state. Therefore, a natural approach is to change the system so that $f(t) = 0$ to a sufficient accuracy at all times. In the case of inductive coupling of a pulsed electromagnet to another, one has $f(t) = -MdI_{\text{p}}/dt$, where nulling the mutual inductance $M$ eliminates the transient without a need of changing the current in the pulsed coil.

In principle, any pair or combination of coils in the system can be decoupled from each other with additional transformers. For instance, toroidal transformers could be used, which in principle do not create the magnetic fields on the outside, and therefore could be even inside the MSR. With air-cored transformers one avoids frequency dependencies, phase shifts, and dissipation in the core, though high mutual inductances are more easily achieved using highly permeable cores.

Despite the elegance of separate decoupling transformers, they are not always the best option. First, they increase the total inductance seen by the current sources used, which may result in reduced slew-rate, narrower

bandwidth, or instability. Second, high currents and voltages in coils give additional requirements to the transformer. The resistance of the transformer coils may significantly increase the on-state voltage needed, whereas the power dissipation may necessitate cooled transformer coils. Superconducting transformers, possibly in a separate cryostat, may also be considered, but this would add to the complexity of the system.

In some cases, it is possible to design the coils themselves in such a way that the produced magnetic fields meet the requirements, but the mutual inductance is zero. An example of such a coil was made in this work, as will be explained in Section 4.4. The main idea is to add extra turns in one coil that have strong coupling to another, canceling the mutual inductance, while the effect on the field in the imaging volume is acceptable.

Extending the concept of zero-mutual-inductance coil design, coupling between the pulsed coils and the MSR can be canceled by the same principle. However, as an additional complication, the MSR in reality is not a single coil, but has infinitely many possible current paths. Again, an ideal toroidal coil produces no field on the outside. Such a coil was used in initial tests at Aalto University to protect non-field-tolerant SQUIDs from $\vec{B}_\mathrm{p}$ pulses [27]. It was wound around a fixed water sample for testing. To allow larger and replaceable samples or human subjects, another design is needed.

For an essentially circular, dipole-like polarizing coil, a solution is to use a larger shielding coil in series with the actual coil, with the current flowing in the opposite direction. The dipole moment per unit current of a circular coil of radius $R$ and $N$ turns is $\pi R^2 N I$. A shielding coil of, for instance, twice the radius and a quarter of the number of turns compared to the actual coil would make the total dipole moment of the coil vanish. The field from a circular coil of radius $R$ and $N$ turns is $\mu_0 N I / 2R$ at the center, resulting in a decrease of the polarizing field by only $1/8$ of the unshielded amplitude. Also the total inductance would increase by no more than tens of percent. Further increasing the size of the shielding coil would yield even smaller changes in these properties. The described approach has been successfully used with the Aalto system. The polarizing coil and its series shielding coil can be seen in the center of Fig. 2.3 in orange.

A vanishing dipole moment does not imply zero mutual inductance to all the eddy-current paths in the MSR. Still, the magnetic flux reaching the conducting wall is reduced to a small fraction. In fact, if the two series coils are concentric and lie in a shared symmetry plane, even the quadrupole moment is zero. The field from the resulting octopole decreases with the distance $r$ as $r^{-5}$. For a further improvement, careful positioning of the shielding windings outside the symmetry plane can in principle cancel even the octopole moment and higher moments, as discussed in Ref. [28]. It has

also been shown that, in a spherically symmetric MSR approximation, the dipole moment gives rise to a uniform transient field inside the room, while a quadrupolar pulse generates a transient whose field components are linear in space [16]. When dipole and quadrupole moments of the pulsed coil are zero, the field transient at the center of the MSR is zero to first order.

Just as with decoupling transformers for coils, high currents and cooling make the situation more difficult. Shielding coils increase the complexity of coolant flow circuits. Moreover, depending on the ULF-MRI application, there may not be enough space for all the required structures. In highly effective MSRs, significant transients may also arise from, for instance, pulsed gradients, which are more difficult to decouple from the room, because of the larger coil size and more complex geometry. Even with the polarizing coil, zeroing the mutual inductances with all the relevant eddy-current modes to a sufficient accuracy can be difficult. Therefore, despite the elegance of nulling mutual inductances, further understanding of the transient behavior of the system is required. In the following, I will discuss theory related to understanding transients in general and to eliminating them in the MSR or in other parts of the system.

## 3.2   Transients in linear systems

Zeroing the input term in Eq. (3.1) is a sufficient condition for not leaving transients after pulsing. However, as discussed above, that is not always a feasible solution. Additionally, there are systems such as the gradient amplifiers, in which one input term is the controlling signal to be reproduced as a current. Fortunately, zero input is not a necessary condition for not leaving unwanted transients. In this section, I first formulate a fairly general transient issue by adapting theory for linear dynamic systems. Building on the theory, I then propose a method for suppressing unwanted transients based on their dynamic behavior.

### 3.2.1   Linear differential equations

Consider first an $n^{\text{th}}$ order linear differential equation of the form

$$\frac{d^n}{dt^n}x(t) + c_{n-1}\frac{d^{n-1}}{dt^{n-1}}x(t) + \ldots + c_1\frac{d}{dt}x(t) + c_0x(t) = f(t) \, , \qquad (3.3)$$

which is an extension to the first-order version seen in Eq. (3.1). As before, the transient after a pulse in $f(t)$ is determined by the homogeneous equation ($f(t) = 0$) along with the initial condition for $x(t)$ and its derivatives up to

order $n - 1$. The general solution for the homogeneous equation is obtained using the ansatz $x(t) = Ae^{\lambda t}$, which leads to the characteristic equation

$$\lambda^n + c_{n-1}\lambda^{n-1} + \ldots + c_1\lambda + c_0 = 0 \ , \qquad (3.4)$$

where the left-hand side is called the characteristic polynomial. In a typical realistic case, the polynomial has $n$ separate roots, $\lambda_1, \lambda_2, \ldots, \lambda_n$, and the solution for Eq. (3.3) is

$$x(t) = \sum_{k=0}^{n} b_k e^{\lambda_k t} \ , \qquad (3.5)$$

where the coefficients $b_k$ can be determined from the initial condition. Each real root $\lambda_k$ corresponds to an exponential timescale, whereas each pair of complex-conjugate imaginary roots leads to a sinusoidal oscillation with an exponentially varying amplitude. Stable systems, *i.e.*, where transients decay in a finite time, have $\mathrm{Re}\,\lambda_k < 0$ for all $k$. The time constants are given by $\tau_k = (-\mathrm{Re}\,\lambda_k)^{-1}$. The angular frequency of the additional oscillation is given by $\omega_k = |\mathrm{Im}\,\lambda_k|$. Unstable systems are not relevant to this work, and $\mathrm{Re}\,\lambda_k < 0$ is assumed.

For instance, setting $n = 2$, $c_1 = 2\zeta\omega_0$, and $c_0 = \omega_0^2$ gives the equation of a damped harmonic oscillator with damping factor $\zeta$ and undamped frequency $\omega_0$. An example of this case is a parallel RLC circuit, for which $\omega_0 = (LC)^{-1/2}$ and $\zeta = \sqrt{L/C}/2R$. In an ULF-MRI setup, such a system is formed when oscillations of a coil of inductance $L$ with its own effective capacitance $C$ are damped with a parallel resistor. When the resistor is absent, or its value $R$ is large, so that $\zeta < 1$, the system is underdamped. In this case, the coil, when disconnected after a pulse, can exhibit decaying oscillations and produce a likely unwanted field. When $\zeta > 1$, the transient is a sum of two exponential decays, the time constants of which increase with decreasing $R$. The transient is at its shortest when $\zeta = 1$, which is called critical damping. In practice, the condition is never met exactly, but in theory, the characteristic equation has then just one double root $\lambda = \omega_0$, and the general solution is $(b_1 + b_2 t)e^{-\omega_0 t}$. The transient thus decays at a timescale given by $1/\omega_0$, which, for a 100-mH polarizing coil with an effective 10-nF capacitance, is 10 µs. The resistance of the coil itself was assumed small, which slightly changes the optimum parallel resistance, since some damping is already given by the finite series resistance.

It has now been shown that linear differential equations with constant coefficients result in a sum of exponential decays and damped oscillations, which are indeed the transient types observed in practice. If the $n$ significant exponential and sinusoidal modes in a transient are identified, one obtains corresponding values for $\lambda_k$, and a homogeneous differential equation can be found by first constructing the characteristic polynomial as $\prod_{k=1}^{n}(\lambda - \lambda_k)$,

which directly leads to the coefficients $c_k$ when expanded. However, one has no control over the amplitudes of the transient modes. Hence, Eq. (3.3) is not a sufficient model in general. Even if the homogeneous equation could explain the transient, a major limitation would still be that the input term $f(t)$ only describes one type of coupling to the transient modes.

## 3.2.2 Linear system with $n$ internal degrees of freedom

A more general model is obtained by representing the state and input of the system as $n$-vectors $\boldsymbol{y}(t)$ and $\boldsymbol{g}(t)$, respectively, and defining the dynamics by

$$\frac{d}{dt}\boldsymbol{y}(t) = \boldsymbol{A}\boldsymbol{y}(t) + \boldsymbol{g}(t) , \qquad (3.6)$$

where $\boldsymbol{A}$ is an $n \times n$ matrix. Like Eq. (3.3), this system is time-invariant, which means that the coefficient matrix $\boldsymbol{A}$ is constant. The response to an input is thus independent of what time instant the input is given at. However, things such as external temperature fluctuations may slowly affect the properties of the system, $i.e.$, matrix $\boldsymbol{A}$. Especially in electronics, the system can also be purposely changed in the sequence, for instance, by disconnecting a coil from its amplifier during data acquisition. Still, it is usually convenient to use the time-invariant model.

In contrast to Eq. (3.3), the input $\boldsymbol{g}(t)$ and output $\boldsymbol{y}(t)$ in Eq. (3.6) are now both $n$-vectors instead of scalars. Scalar inputs and outputs can be made compatible by setting

$$\boldsymbol{g}(t) = f(t)\boldsymbol{p} \quad \text{and} \quad x(t) = \boldsymbol{q}^*\boldsymbol{y}(t) , \qquad (3.7)$$

where $^*$ denotes the conjugate transpose. The scalar input $f(t)$—such as the current in the polarizing coil—couples to system degrees of freedom through the coefficient vector $\boldsymbol{p}$, and the observed output $x(t)$ is now a linear combination of the state variables in $\boldsymbol{y}(t)$, with the values in $\boldsymbol{q}$ determining the coupling. Examples of outputs are the current of a coil and a transient field component at a given point. Generally, the system can have any number of inputs and outputs, which can be easily added to the model if needed.

The connection of this improved model to Eq. (3.3) is found by choosing

$$\boldsymbol{A} = \begin{bmatrix} 0 & 1 & 0 & \cdots & 0 \\ 0 & 0 & 1 & & 0 \\ \vdots & \vdots & & \ddots & \\ 0 & 0 & 0 & & 1 \\ -c_0 & -c_1 & -c_2 & \cdots & -c_{n-1} \end{bmatrix} \quad \text{and} \quad \boldsymbol{y}(t) = \begin{bmatrix} x(t) \\ x'(t) \\ \vdots \\ x^{(n-2)}(t) \\ x^{(n-1)}(t) \end{bmatrix} \qquad (3.8)$$

and, for the input and output ($^\top$ denoting the transpose),

$$\boldsymbol{p} = \begin{bmatrix} 0 & \cdots & 0 & 1 \end{bmatrix}^\top \quad \text{and} \quad \boldsymbol{q} = \begin{bmatrix} 1 & 0 & \cdots & 0 \end{bmatrix}^\top , \tag{3.9}$$

which gives Eq. (3.3). Hence, the model in Eqs. (3.6) and (3.7) is truly more general than Eq. (3.3).

The well-known solution to Eq. (3.6) is

$$\boldsymbol{y}(t) = e^{t\boldsymbol{A}}\boldsymbol{y}(t_0) + \int_{t_0}^t e^{(t-s)\boldsymbol{A}}\boldsymbol{g}(s)\,ds , \tag{3.10}$$

if $\boldsymbol{y}(t_0)$ is a known initial condition. The first term is the solution for the homogeneous equation, and the second term can be used for studying how the input pulses excite the transient modes. In the latter case, assuming the system is stable, it is also reasonable to set $\boldsymbol{y}(-\infty) = \boldsymbol{0}$, since the past of the system is effectively forgotten within an interval several times the largest time constant in the system. In fact, $\boldsymbol{G}(t,s) = e^{(t-s)\boldsymbol{A}}$ ($t > s$) is the causal Green's function for Eq. (3.6), or, in signal processing terminology, $e^{t\boldsymbol{A}}$ is the causal impulse response of the system.

Assume $\boldsymbol{A}$ diagonalizes as $\boldsymbol{A} = \boldsymbol{S}\boldsymbol{\Lambda}\boldsymbol{S}^{-1}$, where $\boldsymbol{\Lambda} = \text{diag}(\lambda_1, \lambda_2, \ldots, \lambda_n)$, and $\lambda_k$ ($k = 1, 2, \ldots, n$) are the $n$ eigenvalues of $\boldsymbol{A}$. Corresponding eigenvectors $\boldsymbol{s}_k$ are the columns of the invertible matrix $\boldsymbol{S} = \begin{bmatrix} \boldsymbol{s}_1 & \boldsymbol{s}_2 & \cdots & \boldsymbol{s}_n \end{bmatrix}$. Now, the solution takes the form

$$\boldsymbol{y}(t) = \boldsymbol{S}e^{t\boldsymbol{\Lambda}}\boldsymbol{S}^{-1}\boldsymbol{y}(t_0) + \boldsymbol{S}\int_{t_0}^t e^{(t-s)\boldsymbol{\Lambda}}\boldsymbol{S}^{-1}\boldsymbol{g}(s)\,ds . \tag{3.11}$$

Given the scalar input $f(t)$, the scalar output $x(t)$ is obtained from

$$\begin{aligned} x(t) &= \boldsymbol{q}^*\boldsymbol{S}\left( e^{t\boldsymbol{\Lambda}}\boldsymbol{S}^{-1}\boldsymbol{y}(t_0) + \int_{t_0}^t e^{(t-s)\boldsymbol{\Lambda}}\boldsymbol{S}^{-1}\boldsymbol{g}(s)\,ds \right) \\ &= \tilde{\boldsymbol{q}}^*\left( e^{t\boldsymbol{\Lambda}}\tilde{\boldsymbol{y}}(t_0) + \int_{t_0}^t e^{(t-s)\boldsymbol{\Lambda}}\tilde{\boldsymbol{p}}f(s)\,ds \right) , \end{aligned} \tag{3.12}$$

where the input and output coupling vectors have been redefined as $\tilde{\boldsymbol{p}} = \boldsymbol{S}^{-1}\boldsymbol{p}$ and $\tilde{\boldsymbol{q}} = \boldsymbol{S}^*\boldsymbol{q}$, respectively, and the system state is $\tilde{\boldsymbol{y}}(t) = \boldsymbol{S}^{-1}\boldsymbol{y}(t)$. Further, the result can be written as a sum

$$x(t) = \sum_{k=1}^n \tilde{q}_k^*\tilde{y}_k(t) , \quad \tilde{y}_k(t) = e^{\lambda_k t}\tilde{y}_k(t_0) + \int_{t_0}^t e^{\lambda_k(t-s)}\tilde{p}_k f(s)\,ds , \tag{3.13}$$

which shows that the transient is in fact a linear combination of $n$ independent exponential modes, where possible pairs of complex-conjugate imaginary eigenvalues lead to oscillating modes. The input couples to each mode

$k$ with the strength given by $\tilde{p}_k$, and the output is a linear combination of the states of the modes. The values of $\lambda_k$ can be interpreted the same way as in the $n^{\text{th}}$-order differential equation. In fact, the characteristic polynomial $\det(\lambda \boldsymbol{I} - \boldsymbol{A})$, whose roots are the eigenvalues $\lambda_k$, is identical to Eq. (3.4), when using $\boldsymbol{A}$ from Eq. (3.8).

### 3.2.3 Dynamic cancellation of transients

I continue by examining the condition for an input pulse $f(t)$ that does not leave a transient. Eventually, this leads to the method I call *dynamic cancellation of transients*.

For convenience, I set $t = 0$ and choose that to be the instant at which the pulse ends. In general, the requirement is that $\tilde{\boldsymbol{q}}^*$ times the integral in Eq. (3.12) over the pulse duration vanishes. A simpler sufficient condition, however, can be expressed as

$$\tilde{q}_k^* \int_{-\infty}^{0} e^{-\lambda_k s} \tilde{p}_k f(s)\, ds = 0 \;, \quad \text{for all } k \;. \tag{3.14}$$

Here, it is assumed that $f(t) = 0$ before the pulse. If the modes are degenerate, *i.e.*, two eigenvalues are equal, transient modes can cancel each other's effects in the output, and the above is then not a necessary condition. However, if the eigenvalues are unique, it becomes also a necessary condition.

Typically, the most harmful transients modes are those that have the longest time constants $\tau_k = -1/\operatorname{Re}\lambda_k$, since they can persist with a high amplitude for a long time after a pulse. Therefore, in practice, it can be sufficient that Eq. (3.14) holds for only some of the modes. Furthermore, even when the system has an infinite number of degrees of freedom, it can be approximated with the finite-$n$ system discussed here. If desired, the system can be constructed by either experimentally identifying the dominant modes and the coupling with the input and output, or from theory.

To suppress the excitation of the harmful modes, one may attempt to design a pulse whose temporal profile is such that the subsequent transient is insignificant. However, one should note that features of the pulse that are shorter in duration than the relevant time constants have only a limited effect on the transient. For $|t\lambda_k| \ll 1$, one has $e^{-\lambda_k t} \approx 1$, and the integral in Eq. (3.14) becomes essentially an integral over the pulse. Therefore, short features that do not contribute much to the integral of the pulse cannot remove the transient. Long-lasting features, on the other hand, may prevent the pulse from performing its task.

At first, it may seem that the above does not directly apply to an EMF induced by a pulsed current $I_\mathrm{p}$ through mutual inductance $M$, where $f(t) \propto dI_\mathrm{p}/dt$ and not $f(t) \propto I_\mathrm{p}$. However, the integral to vanish becomes

$$\int_{-\infty}^0 e^{-\lambda_k t} \frac{d}{dt} I_\mathrm{p}(t) \, dt = \left[ e^{-\lambda_k t} I_\mathrm{p}(t) \right]_{t=-\infty}^0 + \lambda_k \int_{-\infty}^0 e^{-\lambda_k t} I_\mathrm{p}(t) \, dt \; , \qquad (3.15)$$

where integration by parts lead the second form. The first term on the right-hand side is zero assuming that $I_\mathrm{p}$ is zero after the pulse. However, an additional DC offset in $I_\mathrm{p}$ has no effect on the EMF-excited transient.

It is now easily seen that the coupling of a current pulse through an EMF is similar to direct coupling of the pulse. One property of such coupling is that for square pulses that are ramped up and down within short time intervals $t_\mathrm{r}$ such that $|\lambda_k t_\mathrm{r}| \ll 1$, the transient is independent of $t_\mathrm{r}$. Each current ramp gives rise to a transient whose amplitude is proportional to the change in $I_\mathrm{p}$ and independent of the precise shape of the ramp. For pulses much longer than $\tau_k$, the transient after the pulse is solely due to the ramp-down. Conversely, when the length of the pulse approaches zero, the effects of the ramp-up and ramp-down cancel each other, and transient modes with long time constants are eliminated. Unfortunately, simply decreasing the duration of the pulse is often not an option in practice. For instance, with phase-encoding gradients, the integral of the pulse is what matters for MRI; shortening the pulse leads to an increased amplitude. For short pulses, it is indeed the integral that determines also the transient. The same applies to polarizing pulses much shorter than the $T_1$ relaxation times of the sample. More generally, it is difficult to reduce transients by reshaping pulses.

The difficulty described above can be circumvented by keeping the original pulse, $f_0(t)$, intact and applying an additional cancellation pulse $f_\mathrm{c}(t)$ by other means, such that the input coupled to the system is $\boldsymbol{g}(t) = \tilde{\boldsymbol{p}}_0 f_\mathrm{c}(t) + \tilde{\boldsymbol{p}}_\mathrm{c} f_\mathrm{c}(t)$. Here, the coupling coefficient vectors $\tilde{\boldsymbol{p}}_0$ and $\tilde{\boldsymbol{p}}_\mathrm{c}$ may be equal in some cases. This idea of separate coupling was in fact already introduced in Section 3.1 in the context of decoupling transformers and shielding coils, where the goal was to cancel the coupling to the harmful modes $k$ at least approximately, $i.e.$, $\tilde{p}_{0,k} f_0(t) + \tilde{p}_{\mathrm{c},k} f_\mathrm{c}(t) = 0$. For instance, with decoupling transformers, this condition can ideally be true for all $k$, but for shielding coils that is typically not the case.

The concept of zeroing the total input to selected modes at all times is not the optimum in general. In many cases, it will, in fact, lead to an increase in other modes. More flexibility is obtained by reshaping $f_\mathrm{c}(t)$ in such a way that, at the end of the ramp-down, a number of modes has been driven to zero. By features of $f_\mathrm{c}(t)$ at timescales comparable to those of the
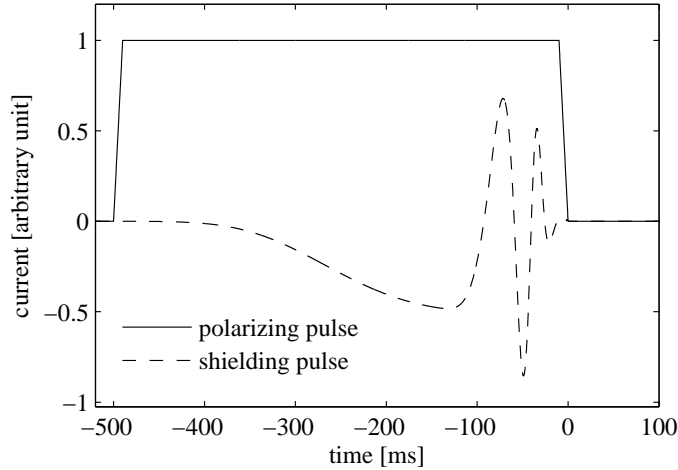
**Figure 3.1:** A dynamic cancellation waveform for a spherical model MSR: modes corresponding to the 12 longest time constants are driven to zero.

unwanted transient, one obtains temporal coupling to the individual modes, extending the instantaneous coupling provided by $\tilde{\boldsymbol{p}}_{\mathrm{c}}$. Using such a *dynamic cancellation* pulse, one can, in principle, cancel transients in any number of modes that correspond to different time constants.

Consider the example of a shielded polarizing coil inside an MSR. As will be explained later, an eddy-current system in a conductive MSR can often be described by a Hermitian operator that has an infinite number of real eigenvalues. Essentially, this leads to multi-exponential transients. From Ref. [16], it is known that, in a spherically symmetric MSR, the different eddy-current modes have a one-to-one relationship with the spherical multipole moments with respect to the center of the room. Further, the time constants decrease with increasing multipole order. This is also roughly true for non-spherical MSRs. Therefore, if some of the lowest-order multipoles are canceled by a larger series-coupled shielding coil, the remaining shorter time constants may be most harmful. In fact, the multipole moments of a coil increase with the coil dimension $R$ as $R^{l-1}$ where $l$ is the multipole order (1 for a dipole, 2 for a quadrupole, and so on). The higher multipoles of the whole series-connected coil are thus likely dominantly from the shielding coil. This is a prime example of where dynamic cancellation is useful.

Figure 3.1 illustrates the simulated use of dynamic cancellation in the spherical MSR model. The polarizing and shielding coils are coplanar and circular with radii $0.1R_{\mathrm{s}}$ and $0.4R_{\mathrm{s}}$, respectively, centered in the MSR of radius $R_{\mathrm{s}}$. Here, both coils have the same number of turns. The shielding pulse waveform is such that all eddy-current modes are driven to zero up to

the mode corresponding to the $l = 12$ multipole moment. With a similar series-connected coil, only the modes up to $l = 2$ would be canceled; in fact, the higher-order eddy-currents would instead be increased because of the series shielding coil.

Suitable shielding waveforms can be found by expressing $f_c(t)$ in a function basis that has at least as many dimensions as the number of modes to be canceled. Suitable coefficients can then be found, for instance, by an iterative optimization algorithm using measurements. The possibility of using extra degrees of freedom, however, is what makes dynamic cancellation very flexible. Using high-dimensional bases such as in Fourier or Wavelet representations, one can add more optimization constraints or goals into the cost function. This allows taking into account concerns such as power, current, or voltage requirements.

In case the polarizing pulse waveform is changed too much by the shielding coil, one can also let $f_0(t)$ change in such a way that the field pulse at the sample remains as intended. Further, one may want to express both $f_0(t)$ and $f_c(t)$ in terms of basis functions, while requiring that the total effect, or field at the sample in the case of a pulsed MRI coil, gives the desired pulse shape.

Further considerations in the method described above include controlling the direct inductive coupling between the shielding coil and the $\vec{B}_p$ coil. To ease the requirements for the current-source electronics, one can decouple the coils from each other using transformers, or as is likely more convenient, by making additional turns in the shielding coil close to the polarizing coil in such a way that the mutual inductance is close to zero. The latter method was implemented in this work in the context of decoupling the $\vec{B}_0$ coil from an additional coil for making the ramp-down of the polarizing field adiabatic in terms of NMR, as described in Section 4.4.

A notable advantage of dynamic transient cancellation compared to in-phase cancellation is that superior transient reduction can be achieved by going beyond limitations given by the coupling strengths of the cancellation input, or coil, to the transient modes. Dynamic cancellation can be generalized to any number of inputs, or coils, with geometries and currents set up to create the desired pulse but no harmful transients. But, as discussed earlier, using a single input and just changing the pulse shape is very limited in applicability. Still, for conventional MRI gradients, eddy current compensation has been done by only reshaping pulses [29, 30]. The technique, however, relies heavily on canceling the effects of the eddy currents instead of reducing the cause; the compensation is added after a ramp, instead of before it. Conventional MRI systems with shielding coils for gradients may also benefit from dynamic cancellation similar to what is described here.

One should note that it is not the linearity of a system that makes dynamic compensation possible. In fact, the main required property is that the system has memory of the recent input to the system. Optimized waveforms could be used for, *e.g.*, controlling hysteretic systems such as ferromagnetic materials or trapped flux in vortices in a superconductor. Such issues do indeed come to play in ULF MRI, for instance, when using a superconducting coil for prepolarization. However, in sufficiently linear systems, the problem becomes simpler in many ways. For instance, it is sufficient to find a shielding waveform for a single step or impulse function, since any waveform can be expressed as a superposition of such functions. Although some of the methods used in the experimental part of this work are related to dynamic cancellation, further development and testing of the method is mostly left for future studies.

### 3.2.4   Filter interpretation

The linear system of Eq. (3.6) can also be interpreted as a filter. In Fourier space, the solution becomes

$$\hat{\boldsymbol{y}}(\omega) = (i\omega\boldsymbol{I} - \boldsymbol{A})^{-1}\hat{\boldsymbol{g}}(\omega) = \boldsymbol{S}(i\omega\boldsymbol{I} - \boldsymbol{\Lambda})^{-1}\boldsymbol{S}^{-1}\hat{\boldsymbol{g}}(\omega) \;, \qquad (3.16)$$

which for the scalar input and output of Eq. (3.7) leads to

$$\hat{x}(\omega) = \sum_{k=1}^{n} \frac{\tilde{q}_k^*\tilde{p}_k}{i\omega - \lambda_k}\hat{f}(\omega) = \sum_{k=1}^{n} \frac{\tilde{q}_k^*\tilde{p}_k\tau_k}{1 + i\tau_k\omega}\hat{f}(\omega) \;, \qquad (3.17)$$

where the second form assumes real eigenvalues. Further, with an inductive input $f(t) = -dF(t)/dt$, the response becomes

$$\hat{x}(\omega) = -\sum_{k=1}^{n} \tilde{q}_k^*\tilde{p}_k \left(1 - \frac{1}{1 + i\tau_k\omega}\right)\hat{F}(\omega) \;. \qquad (3.18)$$

At high frequencies, the output has a phase shift of $\pi$ compared to the input. Therefore, with the right coupling, a linear system can be used for canceling the input. In the next section, it is shown how a conducting MSR can be modeled as such a system, and that the shielded room is in fact a low-pass filter magnetic fields generated by external sources.

## 3.3   Low-frequency eddy currents and shielding

Magnetic shielding by conductive materials is a vast topic, not least because of multiple types of shielding that dominate at different frequency ranges.

At very high frequencies, where the wavelength of the corresponding electromagnetic radiation is small, the interference fields are waves that can be reflected and absorbed by conductive sheets. This makes shielding against radio-frequency interference easy in the sense that even a single thin layer such as household aluminum foil can provide efficient shielding. The difficulty, however, is in that the radiation easily leaks through seams and holes, and can be transferred to the interior of the MSR by wires which act as receiving and transmitting antennas. To solve these issues, pass-throughs for signals, currents, and coolants need to be designed and implemented carefully, and all seams should be conductively bridged.

The transition from shielding at RF to shielding at low ULF-MRI frequencies, however, is complicated. Except for superconductors, conductive shielding does not provide shielding at DC. Going from DC towards higher frequencies, the next regime is where changing magnetic fields induce eddy currents in conductors according to Faraday and Ohm's laws, and currents produce magnetic fields according to the Biot–Savart law. In this section, a model is presented for understanding and analyzing eddy currents and shielding of thin conducting enclosures in this regime.

### 3.3.1   Surface-current model for a thin shield

Consider a thin MSR represented by a piecewise smooth surface $S$, which encloses volume $V$, and the outer normal of which is $\widehat{n}(\vec{r})$ at $\vec{r} \in S$. If a surface current density $\vec{K}$ is assumed to sufficiently describe the currents in the MSR, the system essentially becomes two-dimensional and thus much easier to analyze. However, not all surface current density patterns are physically reasonable. At low frequencies, Maxwell's displacement current $\mu_0\epsilon_0\partial\vec{E}/\partial t$, where $\vec{E}$ is the electric field and $\epsilon_0$ the permittivity of free space, is negligible. Taking the divergence of then valid Ampère's law,

$$\nabla \times \vec{B} = \mu_0\vec{J} \, , \tag{3.19}$$

yields $\nabla \cdot \vec{J} = 0$, which means that the current density $\vec{J}$ should consist of circulating (eddy) currents only.

Further assuming that the eddy currents in $S$ are tangent to $S$, one can write the boundary condition for the magnetic field across $S$ as

$$\vec{B}_+(\vec{r}) - \vec{B}_-(\vec{r}) = \mu_0\vec{K}(\vec{r}) \times \widehat{n}(\vec{r}) \, , \tag{3.20}$$

which follows from the integral form of Eq. (3.19). The subscripts $+$ and $-$ denote limits taken from outside and inside $V$, respectively. Assuming a layer of space with $\vec{J} = 0$ around $S$, one can write the magnetic fields in Eq. (3.20)

using scalar potentials $\Phi_+$ and $\Phi_-$ as $\vec{B}_+ = -\mu_0 \nabla \Phi_+$ and $\vec{B}_- = -\mu_0 \nabla \Phi_-$, which yields

$$\vec{K} \times \hat{n} = -\nabla(\Phi_+ - \Phi_-) = -\nabla \Psi \ , \tag{3.21}$$

where $\Psi = \Phi_+ - \Phi_-$. Since $\vec{K}$ is tangential, this leads to

$$\vec{K} = \nabla \Psi \times \hat{n} \ . \tag{3.22}$$

Clearly, $\vec{K}$ is independent of $\nabla \Psi \cdot \hat{n}$, and $\vec{K}$ can thus be fully described by a scalar function $\Psi$ defined in $S$. A further observation based on Eq. (3.22) is that the eddy currents flow along isocontours of $\Psi$ in $S$. The scalar representation of eddy currents can significantly facilitate theoretical analysis.

While I have shown that any tangential surface current density $\vec{K}$ can be represented using a scalar function $\Psi$, it is still unclear whether all scalar functions $\Psi$ correspond to possible eddy-current patterns. To examine this issue, consider any $\Psi$ and a subset $S_{\mathrm{s}}$ of $S$. The current flowing into $S_{\mathrm{s}}$ through the boundary $\partial S_{\mathrm{s}}$ of $S_{\mathrm{s}}$ is given by

$$\oint_{\partial S_{\mathrm{s}}} \vec{K} \cdot \hat{n} \times d\vec{l} = \oint_{\partial S_{\mathrm{s}}} \vec{K} \times \hat{n} \cdot d\vec{l} = -\oint_{\partial S_{\mathrm{s}}} \nabla \Psi \cdot d\vec{l} = 0 \ , \tag{3.23}$$

where $d\vec{l}$ is a differential path element. Rearranging the scalar triple product and using Eq. (3.21) thus lead to the conclusion that no net current flows into $S_{\mathrm{s}}$. Since $S_{\mathrm{s}}$ is arbitrary, this means that there is no region in $S$ that accumulates charge, and $\vec{K} = \nabla \Psi \times \hat{n}$ is indeed a possible eddy-current pattern.

The surface-current model does not intrinsically take into account the so-called skin effect, in which the assumption of a thin shield apparently breaks down. There are, however, approaches for incorporating the skin effect, as discussed later.

### 3.3.2   Eddy-current basis functions as electric circuits

The scalar representation introduced above is a convenient tool for studying the behavior of the eddy currents in the shield. When the scalar function is expressed in a suitable function basis, the dynamics of the system can be modeled by a coupled system in the basis. Assume the eddy-current pattern in $S$ is given in terms of scalar basis functions $\psi_k$ so that $\Psi = \sum_k j_k \psi_k$, and

$$\vec{K}(\vec{r}, t) = \sum_k j_k(t) \nabla \psi_k(\vec{r}) \times \hat{n}(\vec{r}) = \sum_k j_k(t) \vec{\kappa}_k(\vec{r}) \ , \tag{3.24}$$

where $\vec{\kappa}_k(\vec{r}) = \nabla \psi_k \times \hat{n}$, and $\nabla \psi_k \cdot \hat{n} = 0$. I begin by defining concepts and quantities analogous to those of electric circuits to facilitate such a model.

From Eq. (3.24), the coefficient $j_k$ can be interpreted as the current in circuit $k$. However, the amplitude is not well-defined unless the basis is properly normalized. One way to approach the normalization problem is to consider the ohmic power dissipated in the circuit, which would preferably take the form $R_k j_k^2$, where $R_k$ is the resistance of the circuit. On the other hand, the power dissipated by surface current density $\vec{K}$ per unit area at $\vec{r}$ in $S$ is $K^2(\vec{r})/\sigma(\vec{r})d(\vec{r})$, where $\sigma$ and $d$ are the conductivity and thickness of the shield, respectively. Thus, for $\vec{K} = j_k \vec{\kappa}_k$, the ohmic power dissipation is

$$P = R_k j_k^2 = j_k^2 \oint_S \frac{\kappa_k^2(\vec{r})}{\sigma(\vec{r})d(\vec{r})} \, dS \; . \tag{3.25}$$

Now, if $\sigma d$ is independent of $\vec{r}$, one obtains $R_k = (\sigma d)^{-1} \oint_S \kappa_k^2 \, dS$. Since $(\sigma d)^{-1}$ has the dimension of resistance, it is a good candidate for $R_k$. This corresponds to the normalization

$$\oint_S \kappa_k^2 \, dS = \oint_S (\nabla \psi_k)^2 \, dS = 1 \tag{3.26}$$

and to a general expression for $R_k$:

$$R_k = \oint_S \frac{\kappa_k^2(\vec{r})}{\sigma(\vec{r})d(\vec{r})} \, dS \; . \tag{3.27}$$

Also, with these definitions, $j_k$ has the proper dimension of current.

Now, consider the self-inductive energy of circuit $k$, which is preferably given by $\frac{1}{2} L_k j_k^2$, where $L_k$ is the inductance of the circuit. As with the dissipated power, the inductive energy can be expressed as a surface integral, since the energy per unit area of a surface current $\vec{K}$ is given by $\frac{1}{2} \vec{A} \cdot \vec{K}$, where $\vec{A}$ is the vector potential caused by $\vec{K}$. If $\vec{K} = j_k \vec{\kappa}_k$ and $\vec{A} = j_k \vec{a}_k$, where $\vec{a}_k$ is the vector potential generated by a unit current $\vec{\kappa}_k$, one obtains

$$\frac{1}{2} L_k j_k^2 = \frac{1}{2} \oint_S \vec{A} \cdot \vec{K} \, dS = \frac{j_k^2}{2} \oint_S \vec{a}_k \cdot \vec{\kappa}_k \, dS \; . \tag{3.28}$$

This directly leads to an expression for $L_k$. The self-induced EMF is then given by

$$L_k \frac{dj_k}{dt} = \oint_S \frac{\partial \vec{A}}{\partial t} \cdot \vec{\kappa}_k \, dS = \frac{dj_k}{dt} \oint_S \vec{a}_k \cdot \vec{\kappa}_k \, dS \; . \tag{3.29}$$

Note that $\vec{E} = -\partial \vec{A}/\partial t$ is in fact the induced electric field according to Faraday's law. As can be shown, the coupling of any applied electric field to circuit $k$ is given similarly by

$$e_k = -\oint_S \vec{E} \cdot \vec{\kappa}_k \, dS \; . \tag{3.30}$$

Therefore, the mutual inductance of circuits $k$ and $l$ is

$$M_{kl} = \oint_S \vec{a}_k \cdot \vec{\kappa}_l \, dS = \frac{\mu_0}{4\pi} \oint_S \oint_S \frac{\vec{\kappa}_k(\vec{r}) \cdot \vec{\kappa}_l(\vec{r}')}{|\vec{r} - \vec{r}'|} \, dS \, dS' \, , \qquad (3.31)$$

where the second form comes from expressing the vector potential generated by $\vec{\kappa}_k$ as $\vec{a}_k(\vec{r}) = \oint_S \frac{\mu_0 \vec{\kappa}_k(\vec{r})}{4\pi|\vec{r} - \vec{r}'|} \, dS$.

The mutual inductances, however, do not adequately describe the coupling between the basis functions, since the eddy currents $\vec{\kappa}_k$ share the same conductor. Consider an analogy to simple electric circuits: if a resistor is shared by two electric circuits, a current in one circuit leads to a voltage over the resistor, which is seen as a voltage source by the other circuit. This effect can be viewed as an additional EMF given by Eq. (3.30) with $\vec{E} = -\vec{K}/\sigma d$ opposing the electric field given by Ohm's law. Setting $\vec{K} = j_l \vec{\kappa}_l$, this gives the EMF induced in circuit $k$ by current $j_l$ in circuit $l$. The *mutual resistance* $R_{kl}$ defined by $e_k = R_{kl} j_l$ then takes the form

$$R_{kl} = \oint_S \frac{\vec{\kappa}_k \cdot \vec{\kappa}_l}{\sigma d} \, dS = \oint_S \frac{\nabla \psi_k \cdot \nabla \psi_l}{\sigma d} \, dS \, . \qquad (3.32)$$

Note that Eqs. (3.32) and (3.31) also give the self-inductance and resistance as $R_k = R_{kk}$ and $L_k = M_{kk}$.

### 3.3.3 Dynamics and response of eddy currents

The equation of motion for the eddy currents is found by requiring the total voltage over each circuit $k$ to be zero; $\sum_l (R_{kl} j_l + M_{kl} dj_l/dt + e_k) = 0$, where $e_k$ is an externally induced EMF. Considering $R_{kl}$ and $M_{kl}$ as matrix elements of $\boldsymbol{R}$ and $\boldsymbol{M}$, respectively, this becomes

$$\boldsymbol{M} \frac{d}{dt} \boldsymbol{j}(t) = -\boldsymbol{R} \boldsymbol{j}(t) - \boldsymbol{e}(t) \, , \qquad (3.33)$$

where the components of the state vector $\boldsymbol{j}$ are the currents $j_k$, and those of $\boldsymbol{e}$ are the EMFs $e_k$ given by Eq. (3.34) where $\vec{E}$ is the electric field induced by an applied or interfering magnetic field $\vec{B}_{\mathrm{e}}$ according to Faraday's law.

To obtain a more convenient form for $e_k$, I note that the integrand is $\vec{E} \cdot \nabla \psi_k \times \hat{n} = -\nabla \psi_k \times \vec{E} \cdot \hat{n}$, and that $\nabla \psi_k \times \vec{E} = \nabla \times (\psi_k \vec{E}) - \psi_k \nabla \times \vec{E}$. Using Stokes' theorem, the integral over $\nabla \times (\psi_k \vec{E})$ can be shown to vanish, which leads to

$$e_k = -\oint_S \vec{E} \cdot \nabla \psi_k \times \hat{n} \, dS = \oint_S \psi_k \frac{\partial \vec{B}}{\partial t} \cdot d\vec{S} \, , \qquad (3.34)$$

where $\vec{B} = \vec{B}_{\mathrm{e}}$, and $d\vec{S} = \hat{n}dS$. This also leads to an alternative form for the mutual inductances; since $e_k = M_{kl}dj_l/dt$ when $\vec{B} = j_l\vec{\beta}_l$ is the magnetic field caused by current $j_l$ in circuit $l$, $M_{kl}$ is given by

$$M_{kl} = \oint_S \beta_k^\perp \psi_l \, dS \; , \tag{3.35}$$

where $\beta_k^\perp$ is the normal component of the magnetic field in $S$ produced by a unit current in circuit $k$.

Based on the symmetry of Eq. (3.31), $\boldsymbol{M}$ is Hermitian and therefore has real eigenvalues. Zero is not an eigenvalue of $\boldsymbol{M}$, since the corresponding eigenvector would be a non-zero eddy-current pattern with zero inductance, *i.e.*, zero magnetic field everywhere. Hence, $\boldsymbol{M}$ is invertible, and Eq. (3.33) can be rewritten as

$$\frac{d}{dt}\boldsymbol{j}(t) = -\boldsymbol{M}^{-1}\boldsymbol{R}\boldsymbol{j}(t) - \boldsymbol{M}^{-1}\boldsymbol{e}(t) \; , \tag{3.36}$$

which is of the form of Eq. (3.6) and has a solution according to Eq. (3.10). Notably, the mutual inductance matrix $\boldsymbol{M}$ also affects the coupling of $\boldsymbol{e}$ to the system. The Hermitian resistance matrix $\boldsymbol{R}$ is positive definite, since a negative eigenvalue would violate the second law of thermodynamics, and a zero eigenvalue can only correspond to a superconducting path. Also $\boldsymbol{R}$ is thus invertible for a normal metal shield.

For simplicity, consider a shield with constant thickness and conductivity, or constant $\sigma d$. From Eq. (3.32), it is seen that, if the basis is orthonormal, *i.e.*,

$$\oint_S \vec{\kappa}_k \cdot \vec{\kappa}_l \, dS = \oint_S \nabla\psi_k \cdot \nabla\psi_l \, dS = \delta_{kl} \; , \tag{3.37}$$

the resistance matrix becomes $\boldsymbol{R} = (\sigma d)^{-1}\boldsymbol{I}$. The behavior of the system is now essentially given by the eigenvalues $l_k$ of the inductance matrix $\boldsymbol{M}$ and corresponding orthonormal eigenvectors $\boldsymbol{j}_k$. The characteristic time constant of an eddy-current mode given by $\boldsymbol{j}_k$ is $l_k\sigma d$.

## 3.3.4 From eddy-current modes to shielding

The eigenvectors of $\boldsymbol{M}$ are important also from a shielding point of view. If the eddy currents are represented in the eigenbasis, where $\boldsymbol{M}$ is diagonal, studying the the effect of the shielding eddy currents can become more straightforward. In this section, I study how the MSR shields external interference, assuming the eddy-current basis is readily diagonal and satisfies orthonormality given by Eq. (3.37).

If, additionally, the functions $\psi_k$ are orthogonal in the sense that

$$\oint_S \psi_l \psi_k \, dS = 0 , \quad \text{for } l \neq k , \text{ and} \quad \oint_S \psi_k \, dS = 0 , \qquad (3.38)$$

the mutual inductance matrix, whose elements are given by Eq. (3.35), can be diagonal only if

$$\beta_k^\perp = \alpha_k \psi_k , \qquad (3.39)$$

where $\alpha_k$ is a constant. Further, if the inductances $L_k$ are known, one obtains

$$\alpha_k = L_k \Big/ \oint_S \psi_k^2 \, dS . \qquad (3.40)$$

The above scenario is useful especially because any magnetic field $\vec{B}$ in $V$, when generated by sources not in the interior of $V$, is entirely determined by the normal component $B^\perp = \vec{B} \cdot \widehat{n}$ in $S$. This is because the field can be expressed as $\vec{B} = -\nabla\Phi$, where the magnetic scalar potential $\Phi$ satisfies the Laplace equation $\nabla^2\Phi = 0$; when the normal derivative $\nabla\Phi \cdot \widehat{n}$ has a boundary condition in $S$, the equation has a unique solution in $V$. Here, the boundary condition is $\nabla\Phi \cdot \widehat{n} = -B^\perp$. This motivates expressing the magnetic field in terms of the eddy-current basis functions $\psi_k$, which can be done separately for the external interference field $\vec{B}_\mathrm{e} = -\nabla\Phi_\mathrm{e}$ and the field $\vec{B}_\mathrm{s} = -\nabla\Phi_\mathrm{s}$ generated by eddy currents in the shield.

The applied field takes the form

$$\vec{B}_\mathrm{e}(\vec{r}, r) = \sum_k a_k(t)\vec{\beta}_k(\vec{r}) = -\nabla \sum_k \alpha_k a_k(t)\phi_k(\vec{r}) , \qquad (3.41)$$

where $\phi_k$ is the solution to the Laplace equation with boundary condition $\widehat{n} \cdot \nabla\phi_k = -\psi_k$ in $S$. The EMF induced in circuit $k$ by $\vec{B}_\mathrm{e}$ is then given by

$$e_k = \alpha_k \frac{da_k}{dt} \oint_S \psi_k^2 \, dS = L_k \frac{da_k}{dt} , \qquad (3.42)$$

and the magnetic field caused by eddy currents in the shield is

$$\vec{B}_\mathrm{s}(\vec{r}, t) = \sum_k j_k(t)\vec{\beta}_k(\vec{r}) = -\nabla \sum_k j_k(t)\alpha_k \phi_k(\vec{r}) . \qquad (3.43)$$

From Eq. (3.36) and a Fourier transform solution such as Eq. (3.18), one obtains the scalar potential caused by the shield,

$$\hat{\Phi}_\mathrm{s}(\vec{r}, \omega) = -\sum_k \alpha_k \phi_k(\vec{r}) \left(1 - \frac{1}{1 + i\omega\tau_k}\right) \hat{a}_k(\omega) , \qquad (3.44)$$

where the time constants are $\tau_k = L_k \sigma d$. The Fourier components of the total magnetic field in $V$ then become

$$\hat{\vec{B}}(\vec{r}, \omega) = -\nabla \left[ \hat{\Phi}_{\mathrm{e}}(\vec{r}, \omega) + \hat{\Phi}_{\mathrm{s}}(\vec{r}, \omega) \right] = \sum_k \frac{1}{1 + i\omega\tau_k} \vec{\beta}_k(\vec{r}) \hat{a}_k(\omega) , \quad (3.45)$$

which is a low-pass-filtered version of the applied field $\hat{\vec{B}}_{\mathrm{a}}$. The pass band, however, is different for components of the field that correspond to eddy-current modes with different time constants. As a result, the shielding efficiency depends not only on the frequency $f = \omega/2\pi$ but also on the spatial profile of the applied interference field, and the spatial profile is also affected by the shield.

For the above to hold, it was assumed that the set of basis functions $\psi_k$ that yields a diagonal inductance matrix $\boldsymbol{M}$ satisfies also Eq. (3.38). One example that has this property is a spherical surface $S$ with radius $R_{\mathrm{s}}$ and the *real spherical harmonics* (RSHs) (see Ref. [32]) forming the basis functions $\psi_k$. The RSHs $Y_l^m(\theta, \phi)$ are expressed in terms of the usual complex spherical harmonics $\tilde{Y}_l^m(\theta, \phi)$ as

$$Y_l^m(\theta, \phi) = \begin{cases} 2^{-\frac{1}{2}} \left[ \tilde{Y}_l^m(\theta, \phi) + (-1)^m \tilde{Y}_l^{-m}(\theta, \phi) \right] , & m > 0 , \\ \tilde{Y}_l^m(\theta, \phi) , & m = 0 , \\ 2^{-\frac{1}{2}} \left[ \tilde{Y}_l^{-m}(\theta, \phi) - (-1)^m \tilde{Y}_l^m(\theta, \phi) \right] , & m < 0 . \end{cases} \quad (3.46)$$

These functions have the orthogonality relations

$$\oint_S Y_l^m Y_{l'}^{m'} \, dS = R_{\mathrm{s}}^2 \delta_{ll'} \delta_{mm'} \quad (3.47)$$

and

$$\oint_S \nabla Y_l^m \cdot \nabla Y_{l'}^{m'} \, dS = l(l+1) \delta_{ll'} \delta_{mm'} , \quad (3.48)$$

allowing the eddy-current basis functions to be defined as

$$\psi_l^m(\vec{r}) = \frac{1}{\sqrt{l(l+1)}} Y_l^m(\theta, \phi) , \quad (3.49)$$

satisfying also the orthonormality given by Eq. (3.37). Here, $\theta$ and $\phi$ are spherical coordinates of $\vec{r}$. For convenience, the quantities corresponding to the modes are, instead of a single subscript, indexed with subscript $l$ and superscript $m$, which are integers satisfying $l \geq 1$ and $|m| \leq l$.

The corresponding magnetic field patterns $\vec{\beta}_l^m$ can be found by taking the general solution of the Laplace equation in spherical coordinates [31] in $V$ and outside V and applying boundary conditions at $S$. In $V$, one obtains

$$\vec{\beta}_l^m(\vec{r}) = \frac{\mu_0}{2R_{\mathrm{s}}^l}\frac{l+1}{2l+1}\nabla r^l Y_l^m(\theta,\phi) \ , \tag{3.50}$$

which leads to zero mutual inductances, and self inductances according to

$$L_l^m = \frac{\mu_0 R_{\mathrm{s}}}{2l+1} \ . \tag{3.51}$$

There is no dependence on $m$, *i.e.*, the eigenvalues of the inductance matrix are $(2l+1)$-fold degenerate. The value for $\alpha_l^m$ is found to be $\frac{\mu_0 l(l+1)}{R_{\mathrm{s}}(2l+1)}$. The corresponding time constants are given by the expression

$$\tau_l^m = \frac{\mu_0 R_{\mathrm{s}}\sigma d}{2l+1} \ , \tag{3.52}$$

which is identical with a result obtained from a different approach in Ref. [16]. The time constants can be used in Eq. (3.45) to obtain the field inside the MSR that remains from the external interference field $\vec{B}_{\mathrm{e}}$. The expansion coefficients $a_l^m(t)$ can be obtained from

$$a_l^m(t) = \frac{R_{\mathrm{s}}(2l+1)}{\mu_0\sqrt{l(l+1)}}\oint_S Y_l^m(\theta,\phi)\vec{B}_{\mathrm{e}}(\vec{r})\cdot d\vec{S} \ . \tag{3.53}$$

Similarly, the coefficients can be calculated for a field applied from inside the MSR, since the eddy currents only respond to the normal magnetic field at the shield, regardless of the source. This allows for studying how the MSR also distorts applied magnetic fields.

### 3.3.5  Rectangular shielded rooms

The described theory for eddy currents can be applied to different shield geometries; by parametrizing or discretizing, thin conducting shields of any shape can be analyzed using linear algebra and surface integrals. Even, for instance, multiple-layer MSRs can be studied. While the simple spherical model discussed above can be very helpful in understanding eddy currents in MSRs in general, most practical shields are rectangular.

In the experimental part of this work, a cubic MSR was constructed of rectangular plates which were explicitly not well connected to each other (see Section 4.2). The weakly connected plate-to-plate boundaries are low-conductivity regions of the surface $S$, which, when modeled as such, affect

the dynamics of the eddy currents through the resistance matrix $\boldsymbol{R}$. However, difficulties arise, for instance, from the integrand in Eq. (3.32) becoming nearly singular at plate boundaries. Another inconvenience from allowing $\sigma d$ to vary within $S$ is that the system matrix $\boldsymbol{M}^{-1}\boldsymbol{R}$ becomes non-Hermitian in general, making the analysis more complex both numerically and conceptually.

If the boundaries are considered fully disconnected, these difficulties can be circumvented by selecting a basis for $\Psi$ that is restricted to current patterns that do not cross the plate boundaries. This restriction is equivalent to $\Psi$ being constant along boundaries, *i.e.*, $\vec{K} = \nabla\Psi \times \widehat{n}$ has no component perpendicular to boundaries. For convenience, assume that within all the plate boundaries in $S$, there is a path between any two boundary points. This means that, at all boundaries, $\Psi$ has the same value, which I define to be zero.

One practical basis that satisfies this requirement for a single rectangular plate of dimensions $w \times h$ is a two-dimensional Fourier basis consisting of functions

$$\psi_{nm}(x,y) = \frac{2}{\pi\sqrt{wh\left(\frac{n^2}{w^2} + \frac{m^2}{h^2}\right)}} \sin\left(\frac{n\pi x}{w}\right) \sin\left(\frac{m\pi y}{h}\right) \ , \qquad (3.54)$$

where $0 \leq x \leq w$, $0 \leq y \leq h$, and $n$ and $m$ are positive integers. Any function in the plate that is piecewise continuous, and zero at the edges, has a representation in this basis. If similar basis functions are assigned to all plates in an MSR, all possible eddy-current patterns are covered.

As is straightforward to show, a basis defined this way satisfies the orthonormality condition given by Eq. (3.37). Therefore, if the $\sigma d$ is constant and the same for each plate, the resistance matrix is $\boldsymbol{R} = (\sigma d)^{-1}\boldsymbol{I}$. Now $\boldsymbol{M}^{-1}\boldsymbol{R} = (\sigma d\boldsymbol{M})^{-1}$ is Hermitian, and has real (positive) eigenvalues $1/\tau_k$ in an orthonormal eigenbasis. By calculating $\boldsymbol{M}$ and diagonalizing it numerically, one finds out how the system behaves. After this, it is easy to find the response of the room to any applied field, be it a field pulsed using a coil in the system or an interference signal.

In practice, the values for the indices $n$ and $m$ must be chosen to extend from 1 up to a number that allows a sufficient amount of detail in the eddy-current patterns. The inductances of the modes decrease with $n$ and $m$, and therefore, adding higher-order basis functions adds short time constants into the system. For this reason, adding modes also makes the matrix $\boldsymbol{M}$ increasingly ill-conditioned. Truncating the basis set thus limits the computational complexity as well as increases numerical stability.

Theoretically, however, including basis functions corresponding to large positive integers as $n$ or $m$ is an interesting consideration. As a limit when

summing contributions from all basis functions up to infinite order, one can, in a way, describe any eddy current pattern using this basis, despite the restrictions given on $\Psi$ at the boundaries. Since this may be counterintuitive, an explanation is in order. Although $\Psi$ will always be zero at the boundaries, the value of $\Psi$ can converge to a nonzero value even infinitely close to a boundary line. This can leave a discontinuity in $\Psi$ at the boundary, which leads to a delta function in the component of $\nabla\Psi$ perpendicular to the boundary. This further corresponds to a current within the boundary line. If, on the other side of the boundary, $\Psi$ again has the same nonzero value, the other plate contributes to the boundary current with an equal but opposite current, effectively canceling the current from the one plate.

At high frequencies, the behavior of this model approaches that of a superconducting shield. The validity of this model, however, breaks down when frequencies become high enough to make Maxwell's displacement current significant. Also, when using basis functions of substantially high order, the assumption of a thin shield is no longer valid.

One reason for the breakdown of the thin-shield approximation is that the current density is not uniform across the thickness of the plates, which affects the effective resistance of the eddy-current circuits. This is known as the skin effect, since, at high frequencies, the current tends to concentrate close to the surface of the conductor, within a skin depth. An approach to solving this issue is to model the plates by a number of thin layers with a spacing smaller than the skin depth. Investigating this possibility is left for future work.

The eddy-current model presented here is especially suitable for analyzing unwanted transients, since the number of modes required to describe the essential properties of the transients is relatively small, and computations are efficient. Numerical results based on the model are presented in Section 5.2. The evaluation of Eq. (3.36) was implemented in the eigenbasis of $\boldsymbol{M}$ after numerically integrating the elements of $\boldsymbol{M}$ and calculating the eigenvalue decomposition in MATLAB.

# Chapter 4

# Upgrades to the Berkeley system

The Berkeley system was modified to be compatible with a new and improved polarizing coil that had been added to the Clarke-Group equipment. In Section 4.1, the coil will be described. To overcome the emerging issues, changes were made to the shielding, coil structure, and sequence. These modifications are explained in detail in the following sections.

## 4.1    Water-cooled polarizing coil

Previously, the system was used with a coil wound of litz wire, which consists of many individually insulated thin strands woven together in a carefully designed pattern. The original purpose of such wire is to reduce the additional loss due to the skin effect and the proximity effect at high frequencies. Here, it was used for reducing magnetic noise produced by thermal eddy currents in the conducting coil [24]. The individually isolated strands can only accommodate small current loops, which makes the noise much lower compared to that from a solid wire. Because of the high currents needed for polarization, the coil was pre-cooled with liquid nitrogen.

The coil described above has the limitation that the produced field is high only within a small volume, which is due to the small area of the coil. Moving to a larger coil increases the possible sample size and facilitates the positioning of the sample or subject and the coil in the vicinity of the cryostat. Additionally, a larger copper coil can be positioned in such a way that the noisy copper is not too close to the gradiometer, eliminating the need for litz wire. Now, the coil can be made of copper pipe, in which a coolant, such as water, can flow. This allows for higher polarizing fields even in long uninterrupted MRI sequences.

The new coil, as shown by Fig. 4.1, has 240 tightly packed circular turns
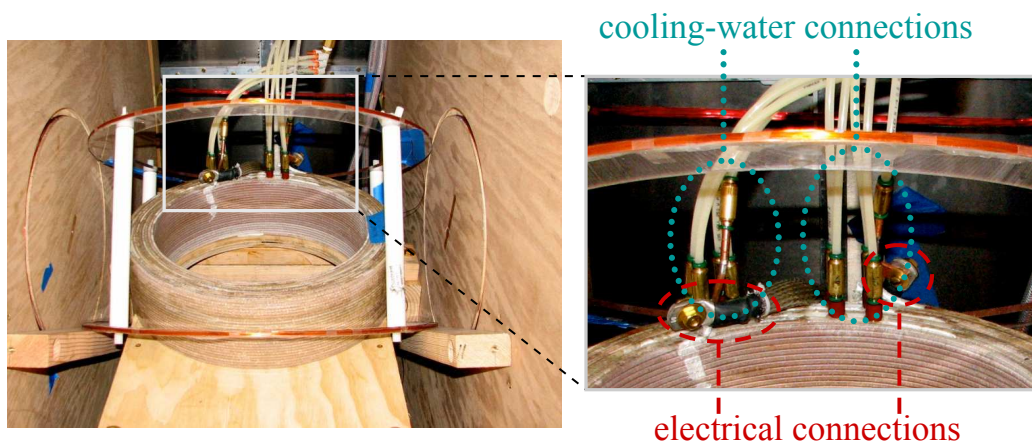
**Figure 4.1:** The water-cooled polarizing coil in place without the cryostat. [23]

of hollow copper wire (or pipe) with a $4 \times 4\,\text{mm}^2$ square cross section. The height of the coil is $11.5\,\text{cm}$, and the inner and outer radii are $16.3\,\text{cm}$ and $20.8\,\text{cm}$, respectively. The coolant path is divided into five parts, which are connected in parallel to decrease the hydrodynamic impedance of the circuit. A 200-A current corresponds to $B_{\text{p}} \approx 150\,\text{mT}$ and a power dissipation of $20\,\text{kW}$ in the coil.

The magnetic dipole moment of the coil at 200 A is large ($5\,\text{kAm}^2$). When ramped to zero in $10\,\text{ms}$ in a quarter-sine-wave fashion, it results in a transient field of over $150\,\mu\text{T}$ in magnitude at the sample, decaying exponentially with a time constant of $50\,\text{ms}$. In addition, the mutual inductance of the polarizing coil with the Earth-field-cancellation coil in the $x$ direction results in a transient current from the electronics of the latter coil, because of an induced EMF in the cancellation coil. A third effect is that $\partial B_{\text{p}}/\partial t$ becomes high enough to reduce the desired adiabaticity of the ramp-down in terms of spin dynamics. All of these effects significantly degrade the ability of the system to function and to produce high-quality images. In the following, solutions to these problems will be described.

## 4.2 Design and construction of shielded room

The previous shielded room, as described briefly in Section 2.5, and to a higher level of detail in Michael Hatridge's Ph.D. thesis (Ref. [24]), was made of 6-mm-thick aluminum plates in a configuration depicted by Fig. 4.2a. The edges and seams were covered from the inside by hollow aluminum bars which constitute the supporting frame of the room. A great number of brass bolts ensured proper electrical contact between the parts and that the shielding
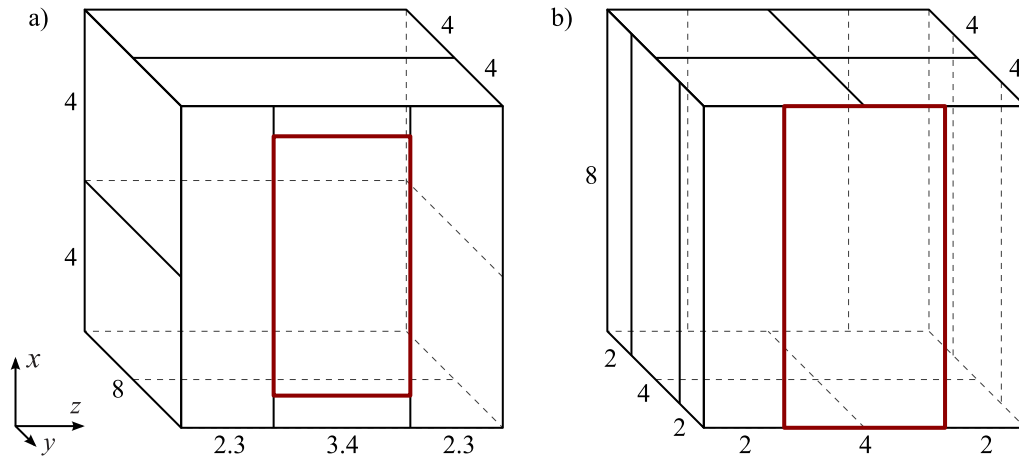
**Figure 4.2:** Schematic of aluminum plates in (a) the old MSR (thickness 6 mm) and (b) the new MSR (thickness 1.6 mm). Dimensions are in ft (0.3048 m). Both cubes measure $2.44 \times 2.44 \times 2.44\,\mathrm{m}^3$ ($8^3\,\mathrm{ft}^3$). Thicker red rectangles depict doors.

efficiency was more than sufficient for ULF MRI.

Since making modifications to a 200-A water-cooled coil would pose a number of difficulties, the coil was assumed fixed, and the eddy-current problem was solved by designing and constructing a new shielded room. It was taken as a goal to build an MSR that provides sufficient shielding at the measurement frequency band but has an eddy-current response small and short enough not to interfere with the MRI scan. As the old shielded room was much more than sufficient, a reduction in the shielding could be tolerated.

As shown in Section 3.3, the shielding is determined by time constants of eddy-current modes in the conducting MSR. The relevant modes depend on the position and nature of the noise sources as well as on the detector. As the details of the sources are mostly unknown, the shield design was made such that the estimated eddy-current transient is just short enough to allow NMR measurement roughly 10 ms after the ramp-down of $B_\mathrm{p}$.

The time constants in the shield can be controlled in two ways. First, decreasing the thickness of the shield brings more resistance in the eddy-current circuits, shortening the time constants. Second, using disconnected or weakly connected plates reduces the sizes of the effective current loops, which removes the modes with the longest time constants. Given that a door in the room already introduces weak connections between plates and that the resistances of connections at the edges of the cube are difficult to regulate, a combination of both approaches was chosen. To keep a high level of symmetry in the design, each of the four sides was divided into individual plates in the same way as the front wall, which has has a door in the middle.

The division is illustrated by Fig. 4.2b.

A high priority was given to symmetry of the MSR for two reasons. Should one, for whatever purpose, require a smaller transient than produced by the MSR, compensation is much easier when the room is highly symmetric. With a $B_\mathrm{p}$ coil centered and aligned with the room, the transient is homogeneous to first order at the center. Such a field can be compensated to a high accuracy in a small volume by using just one compensation coil, or afterwards by means of software. Conversely, a transient from an asymmetric room with its complicated spatio-temporal profile can be difficult even to analyze. The other thing in favor of symmetry is that especially asymmetric shields can imbalance the gradiometer against external fields, *i.e.*, turn an external uniform field into a gradient field detectable by the gradiometer, as discussed in Section 3.3, resulting in an increase in noise instead of shielding.

We also explicitly chose not to divide the wall plates by a horizontal seam for the following reason. As follows from the theory in Section 3.3, and as will be evident from the results in Section 5.1, the transient eddy currents induced by the vertical polarizing pulse do not cross the horizontal symmetry plane. Therefore, a division along that plane would not reduce the transient, but instead impair the shielding. However, carefully chosen horizontal division planes symmetrically around the middle plane might reduce the transient without compromising the shielding.

The new cubic MSR was made the same size as the previous one, that is, $2.44^3\,\mathrm{m}^3 = 8^3\,\mathrm{ft}^3$. Based on measurements of the current paths (see Chapter 5) and on estimations of how the time constants scale with plate dimensions, the thickness was chosen to be a quarter of that of the old shielded room, $1.6\,\mathrm{mm}$ (1/16"). The aluminum alloy used was 6061 with resistivity $1/\sigma = 3.7 \times 10^{-8}\,\Omega\mathrm{m}$ [33]. To keep the plates electrically separate, the supporting frame was made of planed 'two by twos', *i.e.*, wooden bars with a cross section of $38 \times 38\,\mathrm{mm}^2$. The sheet metal was bolted onto the frame using steel bolts, and adhesive tape was used to prevent direct electrical contact from forming between the plates. See Fig. 4.3 for photographs of the MSR.

To make the shield effective against RFI, the narrow slits between the plates were covered by aluminum foil adhesive tape. Further complying with the symmetry requirement, tape with a conducting adhesive was used for the corner seams as well as the seams dividing the ceiling and floor. Before applying the tape, the surfaces were cleaned with vinegar and isopropanol to remove the oxidized surface. The other seams were covered using tape with a non-conductive adhesive. The door plate, which was suspended on four heavy-duty stainless-steel hinges, was RF sealed using a commercial EMI gasket. The gasket is a strip of rubber foam covered with a conducting fabric, such that even a modest pressure will seal the electrical connection

**Figure 4.3:** A photograph of the new magnetically shielded room.

along the full length of the seam.  While one side of the gasket touches the door plate, the other touches a thin aluminum strip that overlaps with both the door plate and the surrounding plates. The strips were kept from direct contact with the surrounding plates by an insulating layer, though RF-sealed to them using aluminum foil tape with non-conductive adhesive. Pass-throughs for coolants and helium gas were implemented by the same wave-guide-type pass-throughs present in the old MSR [24].

## 4.3   Mutual inductance compensations

The MSR effect was not the only harmful $B_\mathrm{p}$-induced transient. The mutual inductance of the polarizing coil and the cancellation coil pair for the $x$ component of Earth's field is significantly high. For high stability and low noise, the DC current source used for the cancellation coils has a slow response. During the ramp-down of the polarizing pulse, an EMF is induced in the cancellation coil. The current source attempts to compensate for the EMF, but cannot keep up with it. After the ramp-down, the EMF is zero, but a current transient remains.

As explained in Section 3.1, this problem could be solved by changing the coil circuits in such a way that the total mutual inductance is zero. However, achieving such canceling coupling to the 200-A polarizing coil without affecting the homogeneity of the Earth's-field cancellation is problematic; an additional coil should be wound in series with the polarizing coil, which is impractical with the high currents. Therefore, another coil not in series with the $B_\mathrm{p}$ coil was used instead. The coil was the primary of a steel-core step-up
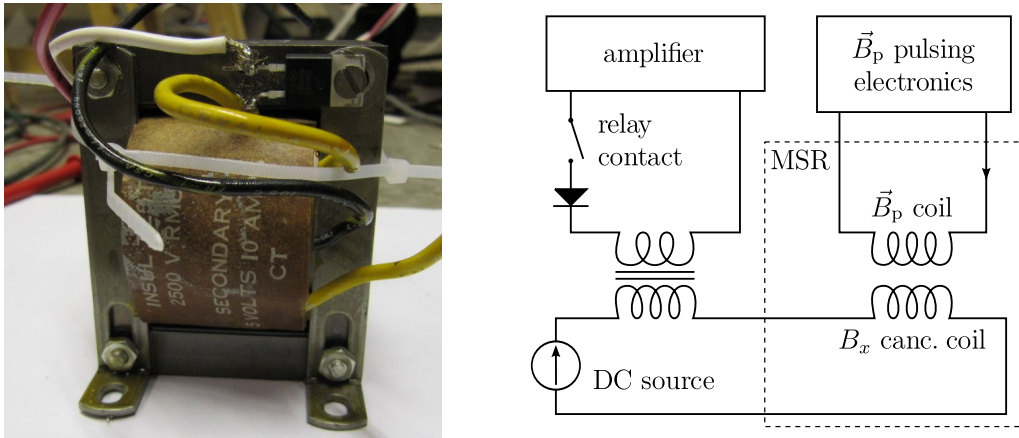
**Figure 4.4:** The transformer used for reducing the $\vec{B}_{\mathrm{p}}$-induced current transient in the $B_x$ cancellation coil. The coupling of the circuits is illustrated schematically.

transformer (Fig. 4.4). The secondary of the transformer was connected in series with the cancellation coil, while current was pulsed into the primary during the polarizing pulse.

Because of eddy currents in the steel core and other effects, the transformer becomes increasingly dissipative at high frequencies. Frequency dependencies of core properties such as the magnetic permeability also introduces rounding and phase shifts in the response. The presence of such effects was evident from the softened shape of the induced EMF in the primary. As the effective pulse shape was not as intended, the fully simultaneous compensation of the $B_{\mathrm{p}}$ pulse did not work properly. To overcome this problem, the current pulse in the transformer was switched off after the ramp-down of $B_{\mathrm{p}}$, and by careful tuning of the current, the transient could be suppressed to a sufficient accuracy. The response of the cancellation coil current source had apparent nonlinearities, and some smaller transients and oscillations remained, but they were small enough to be harmless.

The low-pass-filtering nature of the transformer was in fact a useful property in terms of keeping noise from coupling into the Earth's-field cancellation. However, a diode and a relay were added in series with the secondary to keep the current from going negative, and to keep it zero while not pulsing.

## 4.4    Fixing adiabatic turnoff

The polarizing field, which is perpendicular to $\vec{B}_0$, is designed to be ramped down adiabatically (See Section 2.1). This results in magnetization of the
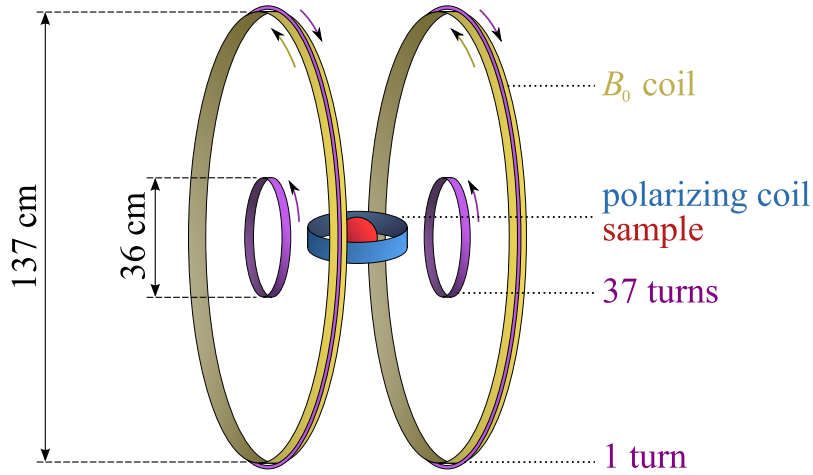
**Figure 4.5:** Additional coil (purple) for ensuring adiabatic turnoff: $2 \times 37$ turns in series with 1 turn around each $B_0$ subcoil (yellow) to cancel the mutual inductance.

sample in the direction of $\vec{B}_0$. Afterwards a $\pi/2$ pulse can be applied to turn the magnetization perpendicular to the measurement field again, which leads to a measurable precession of the magnetization. However, if $\partial B_{\mathrm{p}}/\partial t$ of the ramp-down is increased, the adiabaticity may be broken, leading to a magnetization that is not aligned with $\vec{B}_0$ and precesses with a partial amplitude. A subsequent $\pi/2$ pulse would also just result in a similar partial excitation. This issue was introduced when moving to the new $B_{\mathrm{p}}$ coil with its 10-ms switching electronics.

The adiabaticity condition, Eq. (2.1), is that the rate of change of direction of the magnetic field, $d\theta/dt$, is slower than the precession angular velocity $\gamma B$. Two approaches to making the transition fully adiabatic were considered. One is to slow down the end of the polarizing pulse, as the end is where $d\theta/dt$ reaches its peak and where the precession is slowest. The other is to temporarily increase $B_0$ during the ramp-down such that not only is $d\theta/dt$ decreased, but the instantaneous field magnitude $B$ is increased as well. We chose to implement the latter option.

Because a slow-response DC supply was used for producing a low-noise $\vec{B}_0$ field, an additional coil was made for boosting $B_0$ during $B_{\mathrm{p}}$ ramp-down. The coil arrangement along with the $B_0$ coil is depicted by Fig. 4.5. The additional field need not be very homogeneous, so a pair of small 30-cm-diameter coils with 37 turns each could be used for the purpose. By winding an additional turn on each side around the $B_0$ coil in the opposite direction, the mutual inductance of $220\,\mu\mathrm{H}$ was reduced by two orders of magnitude to $2.6\,\mu\mathrm{H}$. This was enough to prevent notable additional transients from occurring. A current of $18\,\mathrm{A}$ in the coil boosts $B_0$ by $610\,\mu\mathrm{T}$.

# Chapter 5

# Measurements and computations

Measurements of eddy currents in the walls and the resulting transient at the sample were conducted both with the old and new magnetically shielded rooms of the Clarke-Group system. Based on Section 3.3, I present computations for comparison. The effectiveness of the changes made to the system was tested, and, finally, test images were made. In this chapter, I will first describe the methods used in these studies, and then continue with the obtained results.

## 5.1 Methods

### 5.1.1 Transient-field study

At first, it was unclear whether the magnetic field from the eddy-current transient of the old 6-mm MSR was high enough at the sample to disturb the spin dynamics, or if exceeding the SQUID dynamic range was the only problem. Since the SQUID sensor of the system was in a gradiometric configuration, it was not suitable for measuring the transient field. Fluxgate magnetometers are typically used for measuring in field strengths less than $1\,\mathrm{mT}$. The 150-mT pulse, from which the transients results, can leave the ferromagnetic core of the fluxgate magnetized. Therefore, a similarly-shaped 300-ms pulse of only $15\,\mathrm{mA}$ was applied from a controlled voltage source, and the MSR response was assumed to scale linearly with the $B_\mathrm{p}$ amplitude. A resistor was added in series to make the effect of the coil inductance negligible.

Making similar measurements for the new room turned out to be quite problematic. Even though the dynamic range and the nominal bandwidth of the APS 520A fluxgate magnetometer were sufficient for such measurements, the response seemed to have some longer time constants of over $10\,\mathrm{ms}$. This

fluxgate transient was orders of magnitude smaller than the pulsed field, but still several times larger than the MSR transient. Attempts were made to characterize the fluxgate effect and remove it from the measured data afterwards, but the nature of the response seemed to depend strongly on parameters such as the field direction and possibly the gradient. This made results difficult to reproduce.

The above issues are a demonstration of an inherent challenge of ULF MRI, that is, measuring small signals with highly sensitive SQUID sensors after pulses that are many orders of magnitude higher. Ironically, however, the problem was solved by using a SQUID. A high-dynamic-range SQUID magnetometer was put together specifically for this purpose.

To make a DC-SQUID sensor with a high dynamic range, the sensitivity had to be compromised. Instead of an on-chip input coil on top of the SQUID washer, a wire-wound three-turn circular coil with a 3-mm diameter was used. The coil was placed roughly 5 mm away from and in plane with the SQUID, inside a small cylindrical niobium can. The goal was for the input coil to have a low mutual inductance with the SQUID but to still dominate over the external field leaking in from one open end of the can. The pickup coil was made circular with a 25-mm diameter, positionable either vertically or horizontally. The whole flux transformer was made of insulated Nb-Ti wire.

With this setup, the achieved dynamic range was on the order of $100\,\mu\text{T}$, depending on the feedback resistor used. The polarizing coil was pulsed with a 41-V pulse, again with the same shape as an actual polarizing pulse, and through a 2.4-k$\Omega$ resistance. This gave a 17-mA pulse, corresponding to $13\,\mu\text{T}$. The controlled voltage source also produced some unwanted transients much larger than the MSR response. To remove them, a diode was placed in series with the coil, and the voltage was controlled to slightly below zero, leaving the diode in charge of switching off the current. To prevent RFI from entering the system, a filter was added, and the circuit was grounded to the MSR wall. Additionally, the circuit was opened after the ramp-down using a reed relay. To remove the effect of external magnetic-field noise especially at low frequencies, averages were taken over sets of 1000 acquisitions.

For comparison, computations were made according to the method described in Section 3.3.5. Here, a total of 1536 eddy-current modes were used, although 96 modes were able to describe the most essential properties of the transient. The polarizing coil was modeled as a vertically-oriented point dipole at the center of the MSR with a magnitude according to the calculated dipole moment of the actual coil. The numerical integrations and the eigenvalue decomposition were computed using MATLAB.

### 5.1.2  Eddy-current patterns

The nature and severity of the MSR transient problem could be determined by the field measurements described above. However, to better understand the problem, we experimentally mapped the eddy currents themselves. This was achieved by measuring the magnetic field on both the inside and the outside of an MSR wall as a function of time. The wall was considered thin, so that the current could be described by a tangential surface current density $\vec{K}$. Values of $\vec{K}$ were calculated from the discontinuity of the magnetic field using the expression

$$\vec{K} = \frac{1}{\mu_0} \widehat{n} \times (\vec{B}_+ - \vec{B}_-) \,, \tag{5.1}$$

which follows from the quasi-static boundary condition over a surface surrounded by free-space-like medium, $\vec{B}_+ - \vec{B}_- = \mu_0 \vec{K} \times \widehat{n}$ (see Section 3.3.1).

Since the sensor at the wall was not exposed to the full amplitude of the polarizing pulse, the APS 520A fluxgate magnetometer was now suitable. The field was measured along three axes on a grid of points marked on the wall, with each point corresponding to one on the other side. The thickness of the fluxgate enclosure was 25 mm, which adds to the wall plate thickness in terms of separation of the measurement points on different sides of the wall. For the resulting surface current to be accurate, the distance between each pair of measurement points should be small compared to sizes of other conductors or other sources nearby.

The computational model described earlier was used also for calculating the eddy-current patterns in the new MSR.

### 5.1.3  Images

To verify the ability of the system to produce images after the described upgrades, images were made of phantoms such as vegetables and fruit. The sequence used is based on a typical 3D ULF-MRI sequence, *i.e.*, a spin-echo sequence [1] with phase encoding in two directions and frequency encoding in the third. This results in 3D Fourier-encoded data.

Figure 5.1 schematically illustrates the sequence used. Since, in the Berkeley system, the polarizing field is switched off adiabatically and $\vec{B}_1$ pulses are applied, the sequence differs from a corresponding 'high-field' one by only the polarization part and the decay time $T_d$ during which ULF $T_1$ contrast is formed. However, the modifications made for mutual-inductance compensation and adiabatic turnoff (see Chapter 4) add two additional pulses to accompany the actual polarization pulse.
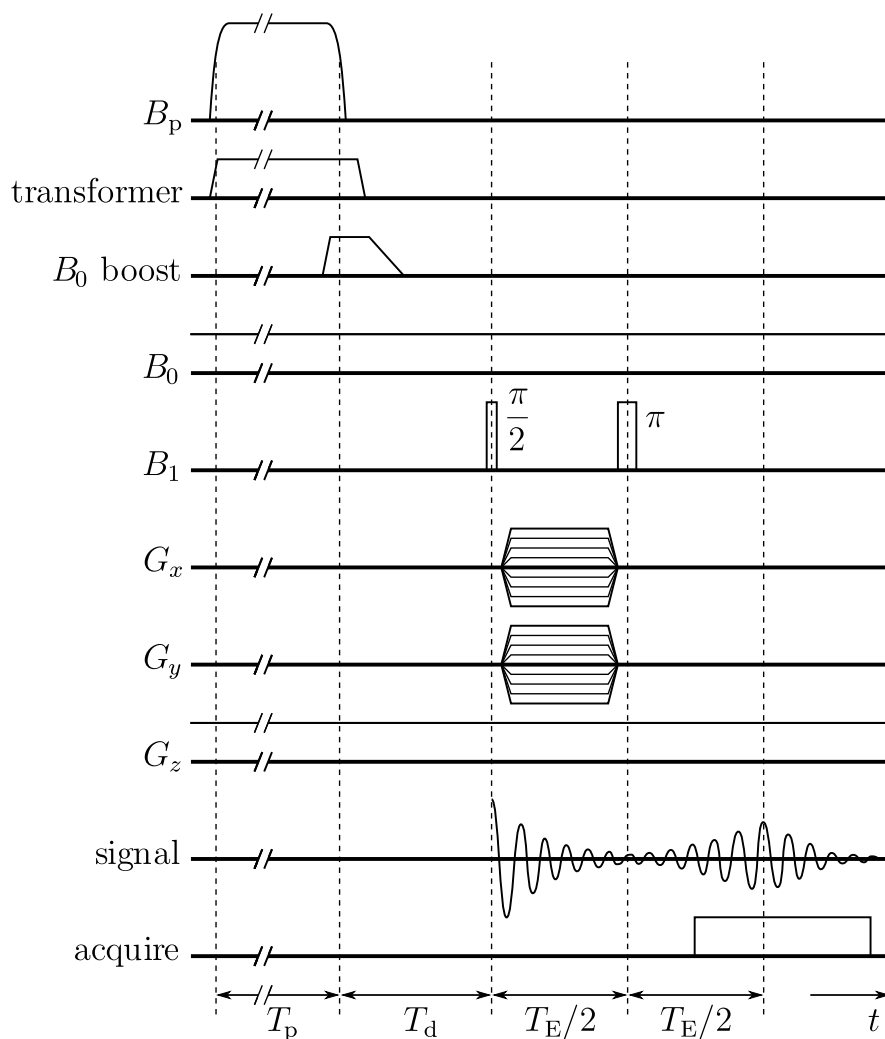
**Figure 5.1:** The spin-echo-based imaging sequence. The changes to a typical ULF-MRI sequence are the compensation pulse fed to the transformer to cancel the effect of the mutual inductance of the polarizing and cancellation coil, and the $B_0$ boost pulse to ensure adiabatic turnoff. Timing values used in all NMR and MRI experiments presented in this chapter are $T_\mathrm{p} = 1\,\mathrm{s}$, $T_\mathrm{d} = 37\,\mathrm{ms}$, and $T_\mathrm{E} = 39\,\mathrm{ms}$.
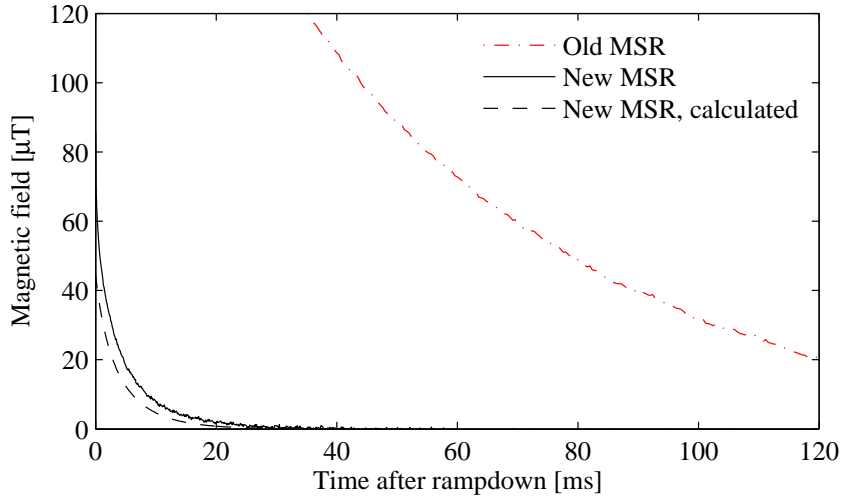
**Figure 5.2:** The $x$ component of the MSR eddy-current field at the sample after pulsing $\vec{B}_{\mathrm{p}} = B_{\mathrm{p}}\widehat{e}_x$ at the center of the MSR in the old an new rooms. Other components are small. Time is measured from the end of the 10-ms ramp-down. The field is scaled to correspond to a 150-mT pulse.

## 5.2   Results

### 5.2.1   Eddy currents

The field transient after a polarizing pulse was massively reduced by upgrading to the new MSR, as is evident from Fig. 5.2. As described in Section 5.1.1, the transient in the old room was measured with a fluxgate and that in the new room with a dedicated high-dynamic-range SQUID magnetometer. Time is defined so that $t = 0$ at the end of the $B_{\mathrm{p}}$ ramp-down. At $t = 30\,\mathrm{ms}$, the eddy currents of the old MSR are still strong enough to cause a field larger than $B_0$. Since the field transient is perpendicular to $\vec{B}_0 = B_0\widehat{e}_z$, this means the field is turned by some 45° from the $z$ axis. The longest time constant of the decaying transient, which was found to be 50 ms by an exponential fit, is on on the same order as $T_1$ times of soft tissues [34]. From this, it is clear that normal operation of the scanner is impaired; by the time the eddy currents have decayed, so has the signal.

According to a similar fit for the new MSR, the dominant time constant there is 6.0 ms. At 15 ms after ramp-down, the transient has decayed to roughly $4\,\mu\mathrm{T}$. Since it is along the $x$ axis, the total field magnitude is then $\sqrt{132^2 - 4^2}\,\mu\mathrm{T} = 132.06\,\mu\mathrm{T}$. The change from $B_0 = 132\,\mu\mathrm{T}$ is approximately a part in 2000, corresponding to a frequency shift of $3\,\mathrm{Hz}$. This is on the same order as the inhomogeneous broadening of the NMR peak of some tissues [34],

and has therefore little effect from an imaging point of view. At 20 ms, the transient is negligible. The calculated response for the new MSR is slightly smaller in magnitude than the result measured with a SQUID. However, the two longest time constants in the simulated transient are 5.8 ms and 6.9 ms, of which the former has the highest amplitude, and is close to the measured value.

The eddy currents themselves were measured using the method described in Section 5.1.2. Results for the old shielded room are depicted by Fig. 5.3. Eddy-current patterns in three of the six faces of the cube were mapped as a function of time, and, from each measured wall, the pattern is shown at two different instants of time. At $t = 2$ ms, the eddy current densities are on the order of $400 \, A/m$. A current as large as roughly 1 kA is found to be circulating horizontally around the MSR. At this point, the currents in the front wall are quite similar to those in the left wall, despite the door that presumably adds a significant amount of resistance along the current paths. Also the currents in the ceiling seem fairly symmetric about the center.

During the transient, the surface-current patterns change significantly. This is because the polarizing pulse excites multiple eddy-current modes that decay at their individual time constants. One notable feature is that the large current across the front wall decays quickly, leaving two small current loops circulating inside the door plate in opposite directions. In the rest of the wall, the currents are visibly flowing around the door to pass through the ceiling and the floor. This is also seen in the ceiling, where a lot of current is concentrated close to the front wall. Further, in the left wall, the currents are already spreading up and down in order to avoid the door. The asymmetry caused by the door is seemingly shifting the effective 'axis of rotation' of the currents towards the back of the MSR.

With time, the currents in the left wall become more evenly spread across the entire height. In the simplest case, this can be explained by a combination of two modes—one nearly uniform mode around the whole cube with a long time constant, and one that consists of current loops within the individual plates. The current loops are counterclockwise above the horizontal symmetry plane and clockwise below it. This follows from the directions in which the magnetic flux lines from the polarizing pulse penetrate the MSR wall. The fact that the current around the whole cube decays more slowly is evidence of the low resistance of plate-to-plate connections.

Similar measurements were done for the new shielded room while most of the MRI instrumentation was not inside. The largely unobstructed access to the wall allowed the use of a finer grid. Figure 5.4 shows the measured eddy-current density (black) at $t = 2$ ms along with a calculated result (blue). As the electrical connections between the plates are negligible, the current
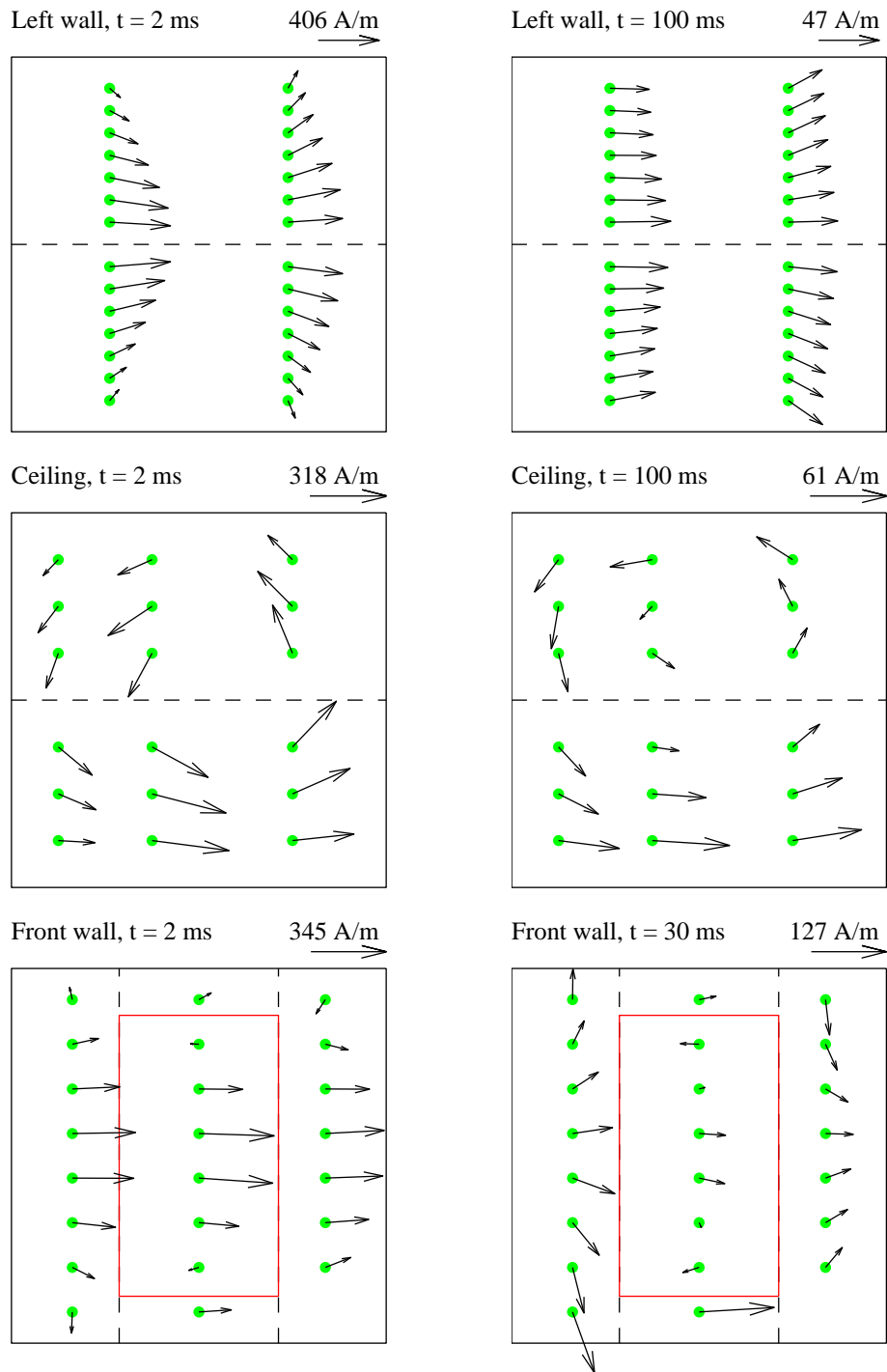
**Figure 5.3:** Surface eddy-current densities at time $t$ after ramp-down of $\vec{B}_\mathrm{p} = B_\mathrm{p}\widehat{e}_x$ pulsed at the center of the old MSR. The measurements are from the left wall, ceiling, and front wall of the MSR (the orientations correspond to Fig. 4.2a). The values are scaled to correspond to a 150-mT pulse.
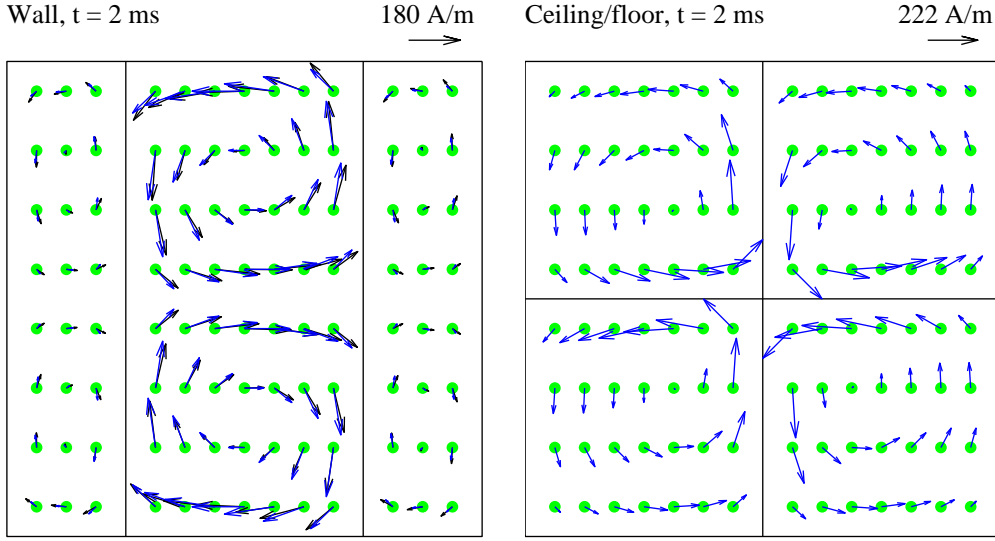
**Figure 5.4:** Surface eddy-current densities with $\vec{B}_\mathrm{p} = B_\mathrm{p}\hat{e}_x$ pulsed at the center of the new MSR. Black arrows are from measurements and blue arrows represent computations. The values are scaled to correspond to a 150-mT pulse.

paths circulating inside the individual plates are dominating. The measured currents in the middle plates decay at a time constant of 6 ms, which is in agreement with the measured transient at the center of the room. The measured and calculated eddy-current patterns are also strikingly similar; the arrows almost perfectly overlap. Similar agreement was found at other values of $t$. Finally, as mentioned in Section 4.2, the currents do not cross the horizontal middle plane. Hence, dividing the plates along the plane would not have decreased the transient but only worsened the shielding.

## 5.2.2 Mutual inductance and adiabatic turnoff

The data in Fig. 5.5 demonstrate the effects of the adiabatic turnoff pulse and the transformer compensation for the mutual inductance of the $B_\mathrm{p}$ coil and the static field cancellation coil in the $x$ direction. The adiabatic turnoff was tested by measuring spin-echo NMR according to the sequence in Fig. 5.1 except for the gradient pulses, which were not applied. Clearly, the NMR spectral peak is much higher when the field pulse from the additional coil described in Section 4.4 is used to ensure fully adiabatic turnoff. Using this method increased the area of the NMR peak by a factor of 2.6. This is because the adiabatic turnoff leaves the magnetization parallel to the $z$ axis, ready for excitation. When omitting the $\pi/2$ excitation pulse in the sequence, the NMR peak was negligible. This means that, with the $B_0$ boost pulse,
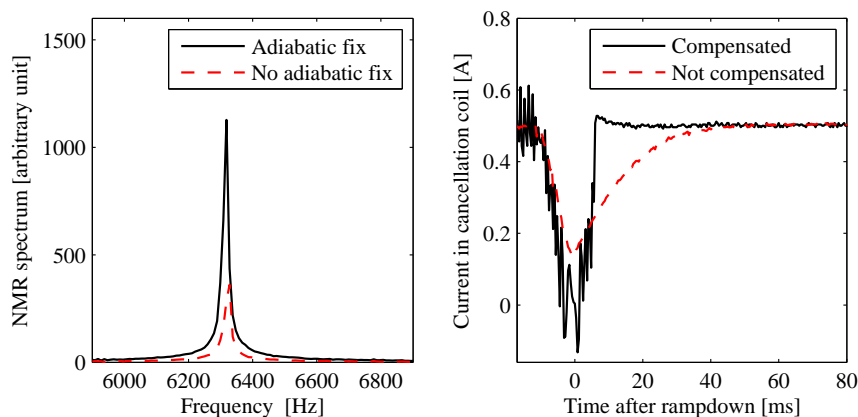
**Figure 5.5:** Test results for (left) the fix for adiabatic turnoff (NMR amplitude spectrum), and (right) compensation for mutual inductance of the polarizing coil and the Earth's field cancellation coil along the $x$ axis.

the level of adiabaticity is sufficient, and no significant component of the magnetization is left in the transverse plane.

The right-hand side of Fig. 5.5 shows the result of the mutual inductance compensation described in Section 4.3. Without the transformer-based compensation (red curve), the ramp-down of the polarizing pulse at time interval $-10\,\text{ms}\ldots 0\,\text{ms}$ brings the current in the compensation coil from $500\,\text{mA}$ to about $130\,\text{mA}$. After this, the deviation in the current decays in $50\,\text{ms}$, which is the transient recovery of the current source used. The transient amplitude corresponds to tens of µT, leading to a significant effect on NMR.

The solid black curve in the figure is the current with the transformer pulse turned on. There is a large amount of noise measured during the transformer pulse, which is eliminated by the series diode after the pulse has been turned off. Most importantly, the remaining transient is only about $30\,\text{mA}$ in magnitude, and decays faster than the original transient. It is another characteristic time scale in the circuit, which could have been eliminated by using a dynamic compensation pulse with two degrees of freedom such as the pulse amplitude and ramp-down time. In this work, however, it was not necessary.[1] The remaining transient corresponds to roughly $2\,\text{µT}$, which is less than the MSR transient.

––––––––––––––––––––

[1]In fact, another cancellation current source was used for images presented in the next section because a voltage limiter was interfering with the compensation. With the other current source, the compensation was implemented similarly, although the remaining transient was more complicated, possibly because of nonlinear effects.
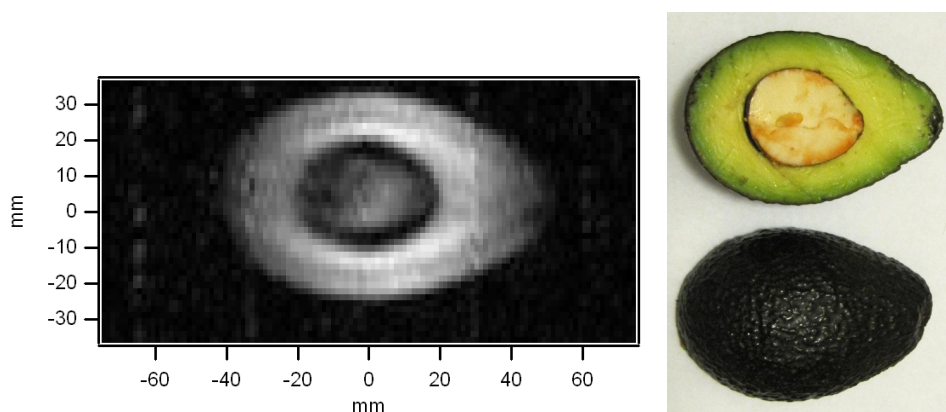
**Figure 5.6:** Cross section of a 3D ULF MRI of an avocado along with a photograph of the same avocado sliced afterwards. The in-plane resolution and slice thickness in the MRI are $2.4 \times 3.3\,\text{mm}^2$ and $7\,\text{mm}$, respectively.

### 5.2.3 Images

To test the system in terms of actual images, some MRI scans according to the sequence described in Section 5.1.3 were performed. Foodstuff was used as samples since the system had not yet been approved for human subjects. The samples were selected with an aim to show contrast not only between air and the sample, but also between different parts of the sample.

Figure 5.6 shows a cross section of a 3D Fourier image of an avocado. Here, the pit is very clearly visible, and the image seems to reveal structure within the green part of the avocado, which is not seen in the photograph. However, the apparent structure may be, for instance, a ringing artefact resulting from $k$-space truncation.

The next image (Fig. 5.7) is a 2D projection of a 3-mm-thick slice of bacon. It is a good demonstration of contrast between different soft tissues; a clear distinction is found between the pixel intensities corresponding to fat (light) and muscle (dark). Especially in this image, vertical noise lines due to harmonics of $60\,\text{Hz}$ are visible. The origin of the harmonics is discussed further in the next chapter.

Finally, Fig. 5.8 shows a cross section of a 3D ULF MRI of a pineapple. One end of the pineapple was cut flat and positioned against the bottom of the cryostat. The MR image shows excellent contrast between the central part and the surrounding area, although the center has only a slightly darker color in the photograph. Similar cases with tissues can be of great value in clinical use, and are what needs to be sought for in order to prove the usefulness of ULF MRI.
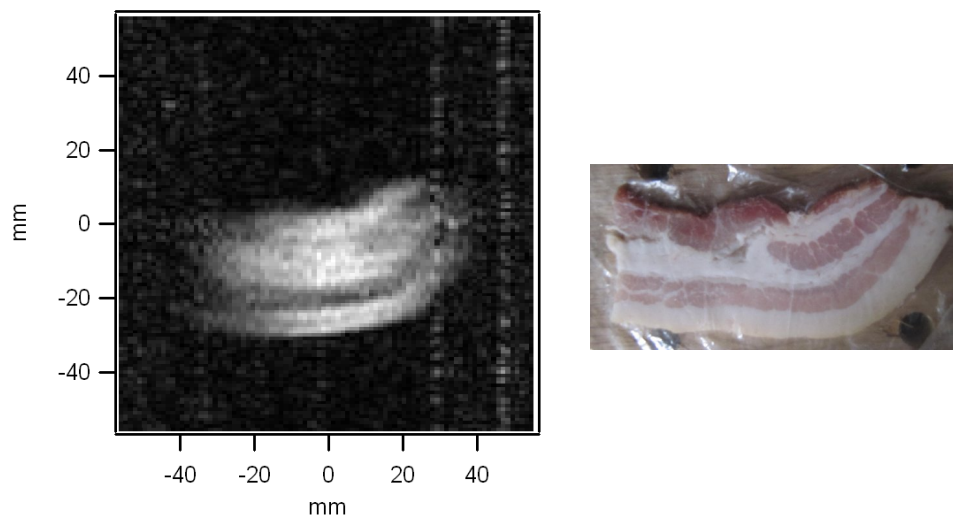
**Figure 5.7:** 2D projection image of a 3-mm slice of bacon along with a photograph of the slice. The resolution of the MRI is $2.4 \times 1.7 \, \text{mm}^2$.
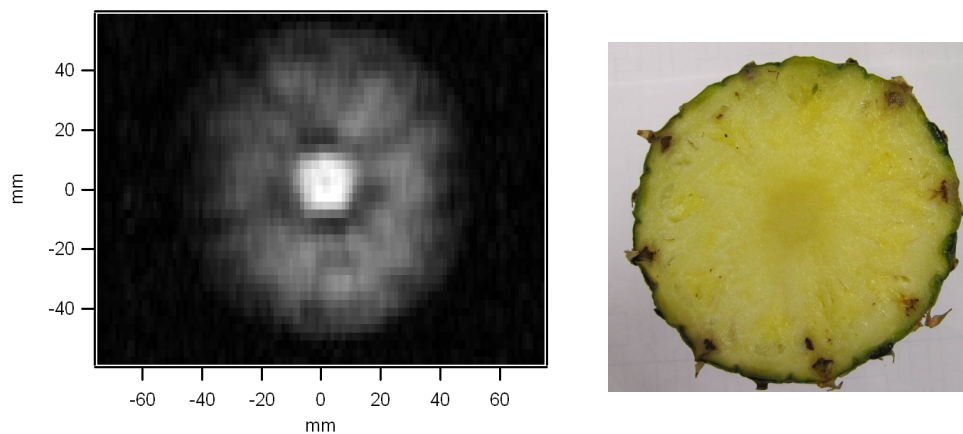


**Figure 5.8:** Cross section of a 3D ULF MRI of a pineapple along with a photograph of the same pineapple. The in-plane resolution and slice thickness in the MRI are $2.5 \times 5.7 \, \text{mm}^2$ and $8 \, \text{mm}$, respectively.

# Chapter 6

# Conclusions and outlook

ULF MRI faces a number of challenges related to the remarkably wide range of magnetic field strengths involved. In this work, I have discussed that many of the challenges in fact stem from a trade-off between low-noise and transient-recovery properties of the setup. This trade-off further results from the overlapping of frequency bands relevant to the signal and the sequence. Most of the issues of harmful transients are, therefore, different faces of the same underlying problem, and can also be solved by variations of the same techniques, such as those presented in this thesis.

Unwanted transients occur in many types of systems, including the eddy-current system of an MSR and the current-supply electronics for a coil. Transients in such systems can, as described in this work, be tackled by three main approaches. In the first approach, the system can be designed so that the energy in the system is quickly dissipated. Examples of this method are damping a self-oscillating coil with a parallel resistor, as well as the new MSR design where plates are thin and weakly connected.

The second approach is to modify the coupling between the pulse that excites the unwanted transient and the transient mechanism. As an example of this, the $B_0$ coil was decoupled from the coil used for ensuring adiabatic turn-off of $B_{\mathrm{p}}$. This is also the approach taken at Aalto, where a series shielding coil is pulsed together with the polarizing coil to cancel most of the coupling to the MSR.

As a third approach, decoupling can be achieved using an additional dimension, time. Indeed, as presented in Chapter 3, the dynamic behavior of transient systems can be exploited to achieve temporal coupling to the transient modes. The decoupling pulses are then time-varying, providing more degrees of freedom for optimizations. The transformer-coupled pulse used for reducing the current transient in the Earth's-field cancellation coil can be considered a very simple example of dynamic cancellation or tem-

poral coupling. By introducing more pulse-shape parameters in tuning the cancellation pulse, transient modes at multiple time scales could have been canceled.

A particularly interesting application for temporal coupling is dynamic shielding of polarizing coils, which extends three-dimensional shielding-coil design to four dimensions. Here, the time constants in the MSR transient correspond to different eddy-current modes, which allows manipulating the spatial profile of the transient by varying the temporal waveform of the shielding pulse. The pulses can, for instance, be designed using a combination of an iterative optimization algorithm and measurements. In addition to more precise transient reduction, this method can also bring more freedom in coil design. By adding constraints or cost terms in the optimization, one can reduce the ohmic power dissipation in the coils, and, for instance, the voltage or current requirements. These interesting prospects are left for further investigation in future studies.

For the first and third approaches, it is very useful to understand the behavior of the transient. In this work, I focused mainly on linear systems, and presented theory of manipulating transients occurring therein. The model of eddy currents in a thin conducting shield (Section 3.3) adapts this theory to a more specific problem. For simple cases such as a spherical shield, the theory provides analytical expressions of shielding performance and transients. Other geometries require numerical computation. However, the use of a Fourier-type basis for the surface currents makes the computation very efficient, since a relatively small number of basis functions is required for transient analysis.

A method was also presented for measuring eddy currents in thin shields. The measurements revealed a total induced current on the order of 1 kA circulating around the old 6-mm-thick MSR after a 150-mT polarizing pulse. Another finding was that the door caused a substantial asymmetry in the eddy currents. In the new MSR, however, the eddy-current patterns reflect the high level of symmetry in the design. The patterns also show a remarkably strong agreement with those obtained from the computational model, which suggests that both the model and the measurement were successful. Therefore, the slight difference between the measured and calculated field transients in the imaging volume is likely to be a transient from the measurement system or from the environment, not from the MSR.

At the 2011 meeting of The International Society for Magnetic Resonance in Medicine (ISMRM), while already finalizing this thesis, I became aware of recent work by Poole *et al.* [35]. In his talk, Poole presented an eddy-current model very similar to that presented in Section 3.3, but applied to currents induced in a cylindrical thermal radiation shield in a more conventional MRI

system. The authors report the advantages of using a Fourier basis as well as even modeling the skin effect by multiple thin layers.

The model can, in principle, be used also for magnetic shielding by eddy currents. However, a considerably larger number of basis functions is required for representing the shielding current to a sufficient accuracy. At a frequency $\omega = 2\pi f$, all time constants on the order of $1/\omega$ and longer can participate in shielding, while transient analysis typically requires only some of the largest time constants. When going to shorter time constants, the required number of basis functions grows rapidly, making the computational complexity and memory requirements too high for standard numerical tools. Numerical studies of the shielding were therefore left for future work. An additional benefit of using the Fourier basis for eddy currents is that the system matrix becomes nearly sparse, *i.e.*, most elements are very small. Based on this property, the numerical calculation can potentially be made very efficient by including the small elements as a perturbation. This could make the model much more feasible for shielding studies.

Based on measurements, the noise levels did not increase when switching to the new MSR, suggesting that the sensor noise was still dominant. However, installing the water-cooled coil and its wirings and electronics introduced some harmonics of 60 Hz in the measured spectrum. The effect is seen in some of the presented MR images as noisy vertical lines. The mechanism by which the interference leaked into the acquired signal remained unclear and subject to further investigations.

The images of foodstuff, however, show excellent contrast between different regions. Pineapple images also demonstrate how the new polarizing coil allows positioning of larger samples or, for instance, a human head in the imaging volume without problems; the imaging volume is now limited mainly by the depth sensitivity of the SQUID. The use of the 150-mT pulses with the new polarizing coil was made possible by the new MSR, which reduced the unwanted field transient by roughly two orders of magnitude at some 15 ms after $B_\mathrm{p}$ ramp-down.

Reducing the noise and increasing the polarizing field remain two main directions in the struggle towards higher-quality images in ULF MRI. As discussed in this thesis, both directions can lead to increased transients, which make it very difficult to measure quickly after a polarizing pulse. On the other hand, one should measure soon after polarization, since that is when the signal is at its highest. Furthermore, in a hybrid MEG-MRI system, even small field sweeps well within the dynamic range of the sensors can be very harmful since they are superposed with the MEG signal, which contains low frequencies down to nearly DC. For these reasons, future systems may benefit from a combination of all three transient-reduction approaches discussed

here, perhaps combined with a fourth approach of tolerating some amount of transients, and compensating for them in signal processing or by active field compensation using additional coils. Having overcome the issue of transients induced by the polarizing pulse, ULF MRI can take significant steps towards image quality that is sufficient for applications.

# Acknowledgement

Once again, I would like to express my gratitude to Professor John Clarke, for providing me with an outstanding and inspiring working environment during my visit at UC Berkeley, and to the other people I mention in the Preface.

# Bibliography

[1] Z.-P. Liang, P. C. Lauterbur, *Principles of Magnetic Resonance Imaging: A Signal Processing Perspective*, IEEE Press Series in Biomedical Engineering, IEEE Press, Piscataway, NJ, USA (2000)

[2] J. Clarke, M. Hatridge, M. Mößle, "SQUID-detected magnetic resonance imaging in microtesla fields", Annual Reviews in Biomedical Engineering, **9**, 389–413 (2007)

[3] V. S. Zotev, P. L. Volegov, A. N. Matlashov, M. A. Espy, J. C. Mosher, R. H. Kraus Jr., "Parallel MRI at microtesla fields", Journal of Magnetic Resonance, **192**, 197–208 (2008)

[4] K. C. J. Zevenhoven, "Performance of sensor arrays for SQUID-detected MRI of the brain", report of special assignment, TKK, now Aalto University, Espoo, Finland (2009)

[5] J. Clarke, A. I. Braginski (Eds.), *The SQUID Handbook*, Wiley-VCH Verlag GmbH & Co. KGaA, Weinheim, Germany (2004)

[6] O. V. Lounasmaa, H. Seppä, "SQUIDs in neuro- and cardiomagnetism: Olli V. Lounasmaa Memorial Issue: Low temperature physics and techniques", Journal of Low Temperature Physics, **135**, 295–335 (2004)

[7] V. S. Zotev, A. N. Matlachov, P. L. Volegov, H. J. Sandin, M. A. Espy, J. C. Mosher, A. V. Urbaitis, S. G. Newman, R. H. Kraus, Jr., "Multi-channel SQUID system for MEG and ultra-low-field MRI", IEEE Transactions on Applied Superconductivity, **17**, 839–842 (2007)

[8] W. Myers, D. Slichter, M. Hatridge, S. Busch, M. Mößle, R. McDermott, A. Trabesinger, J. Clarke, "Calculated signal-to-noise ratio of MRI detected with SQUIDs and Faraday detectors in fields from 10 µT to 1.5 T", Journal of Magnetic Resonance, **186**, 182–192 (2007)

[9] N. Ishikawa, K. Nagata, H. Sato, N. Kasai, S. Kiryu, "Effect of RF interference on characteristics of DC SQUID system", IEEE Transactions on Applied Superconductivity, **3**, 1910–1913 (1993)

[10] R. H. Koch, V. Foglietti, J. R. Rozen, K. G. Stawiasz, M. B. Ketchen, D. K. Lathrop, J. Z. Sun, W. J. Gallagher, "Effects of radio frequency radiation on the dc SQUID", Applied Physics Letters, **65**, 100–102 (1994)

[11] W. Ruder, "New magnetic materials", Proceedings of the IRE, **30**, 437–440 (1942)

[12] D. Cohen, "Large-volume conventional magnetic shields", Revue de Physique Appliquée, **5**, 53–58 (1970)

[13] J. E. Zimmerman, "SQUID instruments and shielding for low-level magnetic measurements", Journal of Applied Physics, **48**, 702–710 (1977)

[14] E. Baum, J. Bork, "Systematic design of magnetic shields", Journal of Magnetism and Magnetic Materials, **101**, 69–74 (1991)

[15] P. E. Magnelind, J. J. Gomez, A. N. Matlashov, T. Owens, J. H. Sandin, P. L. Volegov, M. A. Espy, "Co-registration of interleaved MEG and ULF MRI using a 7 channel low-$T_c$ SQUID System", Applied Superconductivity, IEEE Transactions on, **PP**, 1 (2010)

[16] P. T. Vesanen, J. O. Nieminen, K. C. J. Zevenhoven, Dabek, J. Simola, R. J. Ilmoniemi, "The spatial and temporal distortion of magnetic fields applied inside a magnetically shielded room", submitted to IEEE Transactions on Magnetics (2011)

[17] J. Malmivuo, J. Lekkala, P. Kontro, L. Suomaa, H. Vihinen, "Improvement of the properties of an eddy current magnetic shield with active compensation", Journal of Physics E, **20**, 151–164 (1987)

[18] N. Matter, G. Scott, T. Grafendorfer, A. Macovski, S. Conolly, "Rapid polarizing field cycling in magnetic resonance imaging", IEEE Transactions on Medical Imaging, **25**, 84–93 (2006)

[19] H. C. Seton, J. M. S. Hutchison, D. M. Bussell, "A 4.2 K receiver coil and SQUID amplifier used to improve the SNR of low-field magnetic resonance images of the human arm", Measurement Science and Technology, **8**, 198–207 (1997)

[20] A. Macovski, S. Conolly, "Novel approaches to low-cost MRI", Magnetic Resonance in Medicine, **30**, 221–230 (1993)

[21] R. McDermott, S. Lee, B. ten Haken, A. H. Trabesinger, A. Pines, J. Clarke, "Microtesla MRI with a superconducting quantum interference device", Proceedings of the National Academy of Sciences, of the United States of America, **101**, 7857–7861 (2004)

[22] H. C. Seton, J. M. S. Hutchison, D. M. Bussell, "Liquid helium cryostat for SQUID-based MRI receivers", Cryogenics, **45**, 348–355 (2005)

[23] Adapted with small modifications from original Clarke-Group figures

[24] M. J. Hatridge, *SQUID magnetometry from nanometer to centimeter length scales*, Ph.D. thesis, University of California, Berkeley, Paper LBNL-3694E (2010)

[25] Authors of the schematic and photograph are J. O. Nieminen and J. Dabek, respectively

[26] J. Luomahaara, P. T. Vesanen, J. Penttilä, J. O. Nieminen, J. Dabek, J. Simola, M. Kiviranta, L. Grönberg, K. C. J. Zevenhoven, R. J. Ilmoniemi, J. Hassel, "All-planar SQUIDs and pickup coils for combined MEG and MRI", Superconductor Science and Technology, accepted for publication (2011)

[27] P. T. Vesanen, "Laitteisto magneettiresonanssikuvaukseen matalissa magneettikentissä", Bachelor's thesis, TKK, now Aalto University, Espoo, Finland (2008)

[28] J. O. Nieminen, P. T. Vesanen, K. C. J. Zevenhoven, J. Dabek, J. Hassel, J. Luomahaara, J. S. Penttilä, R. J. Ilmoniemi, "Avoiding eddy-current problems in ultra-low-field MRI with self-shielded polarizing coils", submitted to Journal of Magnetic Resonance (2011)

[29] P. Jehenson and M. Westphal and N. Schuff, "Analytical method for the compensation of eddy-current effects induced by pulsed magnetic field gradients in NMR systems", Journal of Magnetic Resonance, **90**, 264–278 (1990)

[30] J. J. Van Vaals and A. H. Bergman, "Optimization of eddy current compensation", J. Magn. Reson., **90**, 52–70 (1990)

[31] J. D. Jackson, *Classical Electrodynamics*, John Wiley & Sons, New York, USA, 3rd ed. (1999)

[32] E. T. Whittaker, G. N. Watson, *A Course of Modern Analysis*, Cambridge University Press, New York, USA, 4th ed. (1927)

[33] "AA6061", from engineering Fundamentals (eFunda), URL: `http://www.efunda.com/`, May 15, 2011

[34] V. S. Zotev, A. N. Matlashov, I. M. Savukov, T. Owens, P. L. Volegov, J. J. Gomez, M. A. Espy, "SQUID-based microtesla MRI for in vivo relaxometry of the human brain", IEEE Transactions on Applied Superconductivity, **19**, 823–826 (2009)

[35] M. Poole, H. Sanchez Lopez, O. Ozaki, H. Kitaguchi, I. Nakajima, S. Urayama, K.-I. Sato, H. Fukuyama, S. Crozier, "Simulation of gradient coil induced eddy currents and their effects in a head-only HTS MRI magnet", IEEE Transactions on Applied Superconductivity, accepted for publication (2011)